UC Riverside

UC Riverside Previously Published Works

Title

A Statewide InSAR Velocity Map for California Produced by a Comprehensive Large Scale Analysis of ARIA Standard Products

Permalink

https://escholarship.org/uc/item/7g2882p5

Journal

Earth and Space Science, 13(8)

ISSN

2333-5084

Authors

Sangha, Simran S

Funning, Gareth J

Govorcin, Marin

et al.

Publication Date

2026-08-01

DOI

10.1029/2026ea005214

Copyright Information

This work is made available under the terms of a Creative Commons Attribution License, available at https://creativecommons.org/licenses/by/4.0/

Peer reviewed

eScholarship.org Powered by the California Digital Library
University of California

Check for updates

Earth and Space Science

RESEARCH ARTICLE
10.1029/2026EA005214

A Statewide InSAR Velocity Map for California Produced by a Comprehensive Large Scale Analysis of ARIA Standard Products

Simran S. Sangha[1], Gareth J. Funning[2], Marin Govorcin[1], and David P. S. Bekaert[1,3,4]

[1]Jet Propulsion Laboratory, California Institute of Technology, Pasadena, CA, USA, [2]University of California, Riverside, CA, USA, [3]VITO, Flemish Institute for Technological Research, Mol, Belgium, [4]California Institute of Technology, Pasadena, CA, USA

Key Points:

- We present a validated statewide map of secular InSAR surface velocity across California using ARIA-S1-GUNW InSAR products from 2014 to 2023
- Comparison between InSAR and GNSS velocities shows millimeter per year agreement
- Leveraging standard ARIA-S1-GUNW products enables accessible time-series processing and validation via open-source ARIA-tools and MintPy

Supporting Information:

Supporting Information may be found in the online version of this article.

Correspondence to:

S. S. Sangha,
Simran.S.Sangha@jpl.nasa.gov

Citation:

Sangha, S. S., Funning, G. J., Govorcin, M., & Bekaert, D. P. S. (2026). A statewide InSAR velocity map for California produced by a comprehensive large scale analysis of ARIA standard products. *Earth and Space Science*, *13*, e2026EA005214. https://doi.org/10.1029/2026EA005214

Received 16 APR 2026
Accepted 31 JUL 2026

Author Contributions:

Conceptualization: Simran S. Sangha, Gareth J. Funning, David P. S. Bekaert
Data curation: Simran S. Sangha
Formal analysis: Simran S. Sangha, Marin Govorcin
Funding acquisition: Simran S. Sangha, Gareth J. Funning, David P. S. Bekaert
Investigation: Simran S. Sangha, Gareth J. Funning, Marin Govorcin
Methodology: Simran S. Sangha, David P. S. Bekaert
Project administration: Simran S. Sangha, David P. S. Bekaert

© 2026 Jet Propulsion Laboratory, California Institute of Technology and The Author(s). Government sponsorship acknowledged.
This is an open access article under the terms of the Creative Commons Attribution-NonCommercial License, which permits use, distribution and reproduction in any medium, provided the original work is properly cited and is not used for commercial purposes.

Abstract Routine Synthetic Aperture Radar (SAR) acquisitions from the Sentinel-1 constellation enable monitoring of slow surface deformation (millimeters to centimeters per year), yet consistent and accessible pathways for producing validated, user-ready velocity products remain limited. Here we present (a) a statewide Interferometric SAR (InSAR) line-of-sight secular surface velocity map for California derived from standardized Advanced Rapid Imaging and Analysis Sentinel-1 Geocoded Unwrapped Phase (ARIA-S1-GUNW) products spanning 2014–2023, and (b) the details of a scalable processing and validation workflow for producing similar maps. Our workflow leverages several open-source software tools for post-processing of GUNW products, time series analysis, corrections for noise, and removal of earthquakes and transient signals. We apply it to data from nine ascending and descending Sentinel-1 tracks across California, and validate the output against Global Navigation Satellite Systems (GNSS) data. The resulting velocity fields resolve tectonic and anthropogenic deformation signals, including elastic strain accumulation and shallow creep along the San Andreas Fault system, rapid subsidence exceeding 10 cm/yr in the Central Valley, and localized deformation associated with groundwater withdrawal and landsliding. We find millimeter-per-year agreement with GNSS velocities, and estimate typical velocity uncertainties to be ≤1 mm/yr over coherent terrain, increasing locally in regions of strong deformation gradients and/or decorrelation. Our velocity map provides an accessible data set for non-specialists to investigate multiple sources of slow secular deformation across California; our workflow can also be used with GUNW products from the NASA-ISRO SAR (NISAR) mission, enabling the leveraging of that rich data source in the future.

Plain Language Summary Satellite radar observations provide a powerful way to monitor how Earth's surface moves over time, but turning these data into reliable, easy-to-use maps at large scales remains challenging. In this study, we use California as an example to demonstrate how regularly acquired and routinely processed satellite radar data can be used to produce validated maps of ground motion. We analyze observations from the European Commission Sentinel-1 satellites over the period 2014–2023 using standardized Advanced Rapid Imaging and Analysis Sentinel-1 Geocoded Unwrapped Phase (ARIA-S1-GUNW) products, which measure how the ground moves between satellite passes. By combining thousands of these products with time-series analysis methods, we can measure the velocity of motion of the ground, accounting for earthquakes, seasonal signals, and atmospheric effects that can distort measurements. We then compare these velocities with Global Navigation Satellite System (GNSS) station data and find agreement within a few millimeters per year in most areas. The resulting maps capture motion from strain accumulation along the San Andreas Fault system, rapid subsidence in the Central Valley, and localized deformation from landslides and human activity. This approach provides a scalable way to monitor Earth's surface and can be extended to NASA-ISRO SAR (NISAR) satellite observations.

1. Introduction

1.1. InSAR as a Means to Study Slow Deformation

Interferometric Synthetic Aperture Radar (hereafter, InSAR) is a geodetic remote sensing method that uses the differential phase of pairs of radar images to estimate the movement of the Earth's surface (e.g., Bürgmann, Rosen, et al., 2000; Rosen et al., 2000).

Resources: Gareth J. Funning, David P. S. Bekaert
Software: Simran S. Sangha, Marin Govorcin, David P. S. Bekaert
Supervision: Simran S. Sangha, Gareth J. Funning, David P. S. Bekaert
Validation: Simran S. Sangha, Marin Govorcin
Visualization: Simran S. Sangha, Gareth J. Funning
Writing – original draft: Simran S. Sangha, Gareth J. Funning, Marin Govorcin, David P. S. Bekaert
Writing – review & editing: Simran S. Sangha, Gareth J. Funning, Marin Govorcin, David P. S. Bekaert

While large deformation signals, such as large earthquakes or rapid volcano inflation, can be identified within a single InSAR image, or interferogram, noise from the propagation of the radar signal through the ionosphere and troposphere typically obscures the signal associated with slow deformation. This limitation can be overcome by time series analysis over a longer record in time (e.g., Berardino et al., 2002; Ferretti et al., 2001; Hooper et al., 2012; Schmidt & Bürgmann, 2003) in combination with tropospheric correction methods (e.g., Bekaert, Hooper, et al., 2015; Bekaert, Walters, et al., 2015; Fattahi & Amelung, 2015). With these approaches it is possible to use the redundancy in the data to suppress noise and identify surface deformation on the order of millimeters per year, potentially allowing study of a wide range of surficial or shallow subsurface phenomena.

Despite the maturity of such methods, there exist significant barriers for their adoption, particularly by non-expert users. Processing of SAR interferograms can require extensive computational resources, internet bandwidth and storage, and also advanced technical expertise, which can make production of InSAR velocity data prohibitively difficult and limit access to would-be end-users. In this study, we address these barriers by leveraging standardized Advanced Rapid Imaging and Analysis Sentinel-1 Geocoded Unwrapped Phase (ARIA-S1-GUNW) interferograms to develop and validate a consistent, statewide InSAR velocity product for California, and by demonstrating a reproducible workflow that reduces the need for raw SAR processing, enabling broader use of InSAR time-series analysis by non-expert users.

1.2. InSAR Studies of Slow Deformation in California

California, and in particular southern California, with its extensive deserts and cities which are excellent and stable targets for InSAR, has a long history of InSAR studies, including some of the earliest applications of repeat-pass interferometry (e.g., Gabriel et al., 1989; Massonnet et al., 1993). These conditions, which foster high interferometric correlation even for infrequent acquisitions, as was the case for early SAR missions, such as the European Space Agency's ERS and Envisat missions, have made it possible to produce robust and coherent estimates of deformation velocity for multiple locations within California over the past three decades.

A wide range of slow deformation sources in California, both natural and anthropogenic, have been studied in this way, including: interseismic strain accumulation on faults (e.g., Fialko, 2006; Peltzer et al., 2001; Tong et al., 2013; Tymofyeyeva & Fialko, 2015), postseismic poroelastic relaxation (e.g., Fialko, 2004), postseismic viscous relaxation (e.g., Pollitz et al., 2001), fault afterslip (e.g., Floyd et al., 2016; Johanson et al., 2006), secular fault creep (e.g., Bürgmann, Schmidt, et al., 2000; Funning et al., 2007; Schmidt et al., 2005), transient fault creep events (e.g., Lohman & McGuire, 2007; Wei et al., 2009), seasonal and secular changes in groundwater storage (e.g., Bawden et al., 2001; Schmidt & Bürgmann, 2003), coastal subsidence (e.g., Govorcin et al., 2025), hydrocarbon extraction (e.g., Argus et al., 2005; Fielding et al., 1998), geothermal power production (e.g., Vasco et al., 2013), permanent subsurface reservoir compaction (e.g., Miller et al., 2020; Smith et al., 2017), landsliding (e.g., Handwerger et al., 2013; Handwerger et al., 2022; Hilley et al., 2004), and subsidence due to soil settling (e.g., Bekaert et al., 2019; Bürgmann et al., 2006; Shirzaei & Bürgmann, 2018). While these studies have demonstrated the possibilities of InSAR for studying slow deformation processes, the majority of them were targeted at limited geographical areas, or at individual processes, typically due to limited data availability and/or limited computational resources. A statewide data set would potentially allow the study of all of these processes within a single resource.

Since 2014, the Sentinel-1 constellation has provided regular SAR acquisitions over most of Earth's land mass, raising the possibility for global monitoring of natural hazards (e.g., Funning & Garcia, 2019; Salvi et al., 2012; Torres et al., 2012). In California, the typical recurrence interval for repeat coverage is 12 days in both ascending and descending orbits, which for most areas of interest is sufficient for maintaining interferometric correlation. In addition, the 250 km-wide swath of Sentinel-1 in Interferometric Wide-Swath (IW) mode enables statewide coverage of California with 9 tracks. Concomitant improvements in the scale and availability of computational resources and accompanying infrastructure have also improved our ability to deliver such a data set, as we will describe below.

1.3. The ARIA Project and Sentinel-1 Geocoded Unwrapped Phase Products

Prior to the availability of dense satellite-based observations, measurements of surface deformation relied primarily on geodetic techniques such as campaign and continuous Global Navigation Satellite System (GNSS), terrestrial triangulation, precise leveling, and tide gauge records, each of which provides precise but spatially

23335084, 2026, 8, Downloaded from https://agupubs.onlinelibrary.wiley.com/doi/10.1029/2026EA005214, Wiley Online Library on [29/09/2026]. See the Terms and Conditions (https://onlinelibrary.wiley.com/terms-and-conditions) on Wiley Online Library for rules of use; OA articles are governed by the applicable Creative Commons License

23335084, 2026, 8, Downloaded from https://agupubs.onlinelibrary.wiley.com/doi/10.1029/2026EA005214, Wiley Online Library on [29/09/2026]. See the Terms and Conditions (https://onlinelibrary.wiley.com/terms-and-conditions) on Wiley Online Library for rules of use; OA articles are governed by the applicable Creative Commons License

sparse constraints on surface motion (Bock & Melgar, 2016). While these approaches have been essential for studying tectonic and other slow deformation processes, they do not provide the spatially continuous coverage needed to resolve deformation over large regions. InSAR-based approaches address this limitation by providing spatially dense measurements of surface displacement. However, InSAR analyses have historically required substantial expertise and computational effort, and have often been performed on a case-by-case basis rather than as part of systematic, large-scale monitoring efforts.

The ARIA (Advanced Rapid Imaging and Analysis) project arose from efforts to operationalize InSAR and other geodetic imaging methods for natural hazard applications. It is a collaborative effort between the Jet Propulsion Laboratory (JPL) and California Institute of Technology aimed at supporting the local, national, and international hazard science and response communities (ARIA Project, 2026). Initially, ARIA developed capabilities in generating science and urgent response imaging products such as damage and flood proxy maps, based on the decorrelation of InSAR data in response to damage or inundation of the surface (e.g., Ulloa et al., 2020; Yun et al., 2015). These products are intended to improve situational awareness for disaster response. More recently, ARIA has expanded its automated imaging and analysis capabilities to keep pace with the rapidly increasing data volumes generated by the European Space Agency's Copernicus Sentinel-1 constellation and NASA-ISRO's SAR (NISAR) mission.

The ARIA-S1-GUNW product has evolved over the years, initially conceived as part of the "Getting Ready for NISAR" efforts at JPL in collaboration with the Alaska Satellite Facility (ASF). Its development has been further advanced through contributions from the NASA Earth Surface and Interior (ESI), Advancing Collaborative Connections for Earth System Science (ACCESS), NISAR Science Team, and NASA Sea-Level Change initiatives. The ARIA-S1-GUNW adopted an early format aligned with the NISAR mission and now comprises an archive of more than 1.6 million products, covering the Sentinel-1 record across major land-based fault systems, global coasts, and active volcanic regions.

These standardized products provide 90-m resolution InSAR measurements generated using the InSAR Scientific Computing Environment (ISCE2) software and unwrapped via the Statistical-cost, Network-flow Algorithm for Phase-Unwrapping (SNAPHU) algorithm (Chen & Zebker, 2002). Distributed in a Climate and Forecast (CF) compliant NetCDF-4 format, ARIA-S1-GUNW files contain the essential layers for geophysical analysis: unwrapped phase, interferometric correlation, SAR amplitude, and line-of-sight (LOS) geometry. The LOS geometry represents the one-dimensional slant range look vector between the satellite sensor and the ground target. Because the radar images the surface from a side-looking perspective, observed phase changes record a one-dimensional projection of true three-dimensional ground motion along this specific viewing trajectory. A comprehensive overview of the product details, including processing parameters and product metadata definitions are detailed in the official product guide (Alaska Satellite Facility, 2026). Recent versions of ARIA-S1-GUNW products also include tropospheric correction layers derived from high-resolution atmospheric models and radar observations, enabled by developments in the Raytracing Atmospheric Delay Estimation for RADAR (RAiDER) framework. These layers are currently available for a subset of regions and time periods, reflecting ongoing efforts to expand their coverage. The products are systematically processed leveraging the open-source AWS-based HyP3 environment (Hogenson et al., 2020) and are made freely available through the open-access ASF Distributed Active Archive Center (DAAC). In this paper, we leverage this comprehensive archive to produce InSAR deformation time-series and interseismic velocities across California.

2. Data and Methodology

2.1. Data Selection

The state of California is covered by Sentinel-1 SAR data from nine tracks (ascending and descending geometries; Figure 1). All nine tracks are within the footprint of data automatically processed by ARIA. We used all available ARIA-S1-GUNW products covering California, which at the time of this writing are available up to ~mid 2023 at the latest in California (Table 1); however the processing framework would allow the database to be retrospectively extended through to the present day, subject to future funding and data access priorities. This archive includes interferograms with 3 nearest connected neighbors and year-long pairs spanning coherent seasons through late spring and early fall, which is intended to maintain network connectivity for time-series analysis. These annual pairs are preserved strictly to anchor long-term secular trends across stable bedrock and urban

10.1029/2026EA005214

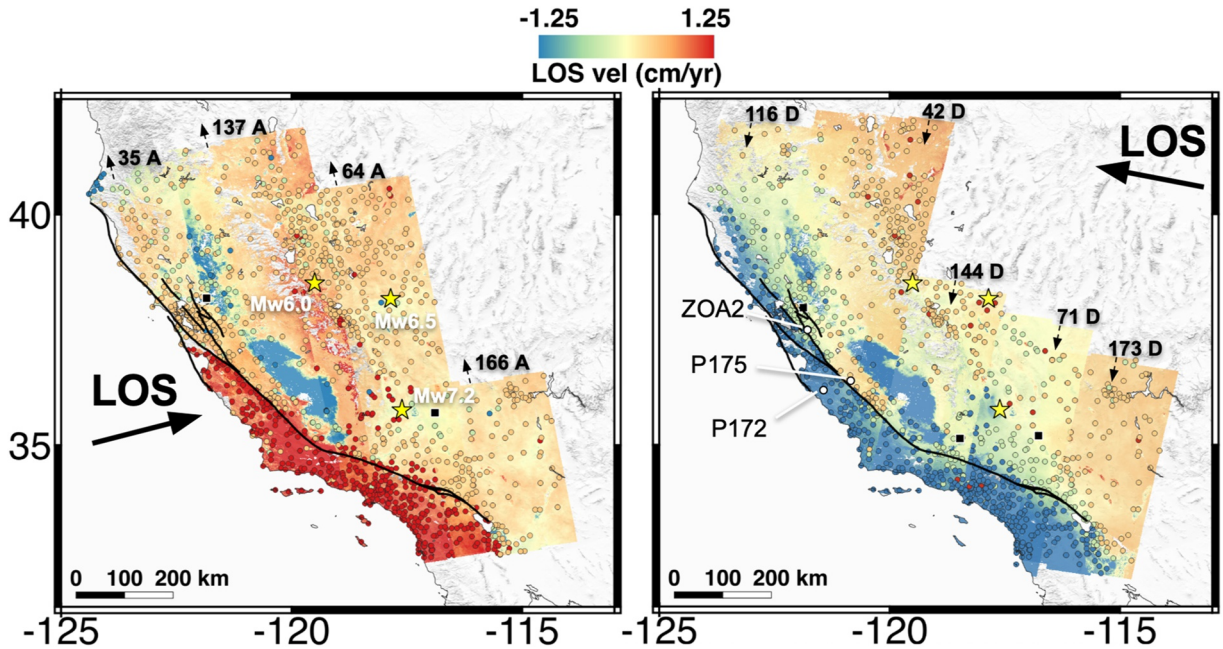


Figure 1. Mosaic of line-of-sight (LOS) surface velocities from ARIA-S1-GUNW InSAR products spanning 2015–2023. Velocities are estimated assuming a linear rate for each Sentinel-1 track (dashed arrows; see Table 1 for track details), corrected for tropospheric noise using weather-model-based corrections, and referenced to a local GNSS station (black squares; see Table 1 for station details). Additional GNSS sites used for comparison are shown as colored markers, with rates estimated over the same time span as the InSAR data. Positive values denote motion of the ground toward the satellite. Coseismic events (yellow stars) are included in the time-series modeling, with the long-term interseismic velocity assumed to remain consistent before and after each event. Traces of major faults (black lines) are from the U.S. Geological Survey (2025a). Background hillshade is from the USGS Shaded Relief Only basemap (U.S. Geological Survey, 2025b), and coastlines and waterbody boundaries are from the National Oceanic and Atmospheric Administration (NOAA) shoreline/coastline database (2025b). General agreement is observed between ascending and descending tracks, with LOS rates consistent with GNSS estimates (see comparison in Figure 6). Minor discontinuities in overlap regions are primarily attributed to differences in viewing geometry between near- and far-range acquisitions. GNSS labels in the right-hand panel correspond to time-series plots shown in Figure 4.

networks, while their influence over rapidly decorrelating agricultural regions is automatically minimized within the time-series inversion based on their low spatial coherence.

Stacks were screened through a routine, single-pass visual quality control check to remove problematic pairs. Interferograms demonstrating pervasive, track-wide decorrelation from heavy winter snow cover across the high Sierra Nevada crest were entirely discarded from the inversion network to safeguard temporal connectivity. For

Table 1
Overview of Sentinel-1 Data Used in This Project

Track number and acquisition geometry	Observation start	Observation end	Number of acquisitions	Number of interferograms	Percentage of valid, unmasked pixels	Reference point lat/lon (collocated GNSS station)
42 D	31/01/2016	04/06/2022	166	921	87.23	37.976/−121.869 (P248)
115 D	10/06/2015	04/05/2022	184	854	81.17	37.976/−121.869 (P248)
144 D	14/01/2016	29/08/2023	277	1,803	89.28	35.143/−118.470 (TEHA)
173 D	04/12/2014	01/06/2022	196	607	98.33	35.205/−116.763 (P615)
35 A	19/01/2016	28/06/2022	227	753	80.38	38.184/−121.844 (P266)
71 D	09/01/2016	06/06/2022	241	1,010	96.62	35.205/−116.763 (P615)
137 A	03/03/2017	29/08/2023	271	1,579	88.52	38.184/−121.844 (P266)
166 A	04/01/2016	21/12/2021	151	696	98.11	35.711/−116.888 (P597)
64 A	14/02/2016	13/05/2022	223	1,120	92.87	35.711/−116.888 (P597)

Note. "A" or "D" refer to ascending or descending acquisition geometries, respectively. Percentage of land pixels masked for each track are also listed. Spatial reference point latitude/longitude and collocated GNSS station name captured.

23335084, 2026, 8, Downloaded from https://agupubs.onlinelibrary.wiley.com/doi/10.1029/2026EA005214, Wiley Online Library on [29/09/2026]. See the Terms and Conditions (https://onlinelibrary.wiley.com/terms-and-conditions) on Wiley Online Library for rules of use; OA articles are governed by the applicable Creative Commons License

23335084, 2026, 8, Downloaded from https://agupubs.onlinelibrary.wiley.com/doi/10.1029/2026EA005214, Wiley Online Library on [29/09/2026]. See the Terms and Conditions (https://onlinelibrary.wiley.com/terms-and-conditions) on Wiley Online Library for rules of use; OA articles are governed by the applicable Creative Commons License

scenes containing only localized, partial snow cover, the frames were retained, and the snow patches were dynamically masked on a pixel-by-pixel basis within MintPy where connected-component values default to zero.

We make use of the open-source ARIA-tools software (Buzzanga et al., 2020) to prepare our interferograms for analysis. ARIA-tools (ARIA-tools, 2026) is an open-source suite of tools that enables downloading, quality-checking, mosaicking, cropping and masking of ARIA-S1-GUNW products in preparation for time series analysis. To exclude unreliable regions of the data—generally characterized by low correlation—we mask the areas which the SNAPHU unwrapper characterizes as not unwrappable (i.e., where the output connected component value is zero and the estimated temporal correlation is low), and also apply a permanent water body mask derived from the European Space Agency WorldCover 2021 product (Zanaga et al., 2022). Of particular importance to this analysis is the mosaicking of the ARIA-S1-GUNWs, each of which covers a single Sentinel-1 frame of fixed size, into the long swaths that cover the whole state of California (Figure 1). For this we use an updated stitching algorithm (Govorcin et al., 2025). Here, connected components refer to discrete patches of pixels that have been unwrapped continuously as a single coherent unit by the automated unwrapping algorithm. Specifically, instead of estimating and applying a single uniform phase shift between successive overlapping frames, our stitching algorithm isolates and resolves the unique phase offsets between individual corresponding connected components spanning the zone of overlap between two overlapping frames. This targeted localized alignment ensures that phase discontinuities associated with an isolated component are addressed, preventing them from warping adjacent coherent blocks as we iteratively extend this computation as necessary to stitch all available frames for a given interferometric pair.

2.2. Time Series Analysis and Reduction of Errors and Biases

We performed a time-series analysis on our stitched ARIA-S1-GUNW interferograms using the open-source Miami INsar Time-series software in PYthon (MintPy; Yunjun et al., 2019) package to estimate average LOS surface velocities along with their corresponding uncertainties. Interseismic displacement rates are estimated by fitting the displacement time series with a functional model consisting of a long-term linear (secular) trend, periodic terms representing annual and semiannual signals, and step functions accounting for coseismic offsets at known earthquake times. Modeling both annual and semiannual frequencies follows established geodetic practice for capturing comprehensive seasonal signals (e.g., Dong et al., 2002). These discrete components account for the joint impacts of regional surface mass redistributions, including atmospheric pressure shifts, snow cover changes, and soil moisture variations, alongside bedrock thermal expansion. This parameterization isolates cyclic fluctuations to prevent seasonal noise from leaking into and biasing the secular linear velocity field. The model has the form

$$Vt + C + A_1 \sin(2\pi t) + B_1 \cos(2\pi t) + A_2 \sin(4\pi t) + B_2 \cos(4\pi t) + \sum_{k=1}^{N} S_k H(t - t_k),$$

where V represents the secular displacement rate (velocity), C is a constant offset, A_1 and B_1 are the amplitudes of the annual periodic terms, A_2 and B_2 are the amplitudes of the semiannual periodic terms, S_k is the amplitude of the kth coseismic step occurring at time t_k, and $H(t - t_k)$ is the Heaviside step function activated at $t = t_k$. Here N denotes the total number of modeled coseismic offsets. MintPy is a powerful time-series analysis package that can produce Small BASeline subset (SBAS) solutions for deformation time series and deformation velocities from interferograms generated by a variety of processors or archives, including stacks of ARIA-S1-GUNWs prepared using ARIA-tools.

As tropospheric water vapor remains the principal source of noise in InSAR data, we continue to leverage troposphere corrections derived from the European Center for Medium-Range Weather Forecasts (ECMWF) Reanalysis v5 (ERA5) model using the open-source Python based Atmospheric Phase Screen estimation (PyAPS) software (Jolivet et al., 2011), and evaluate velocities from the corrected data below (Figure 1). No empirical bilinear or quadratic network-wide deramping was performed during the time-series processing to ensure that true long-wavelength tectonic or regional deformation signals were preserved rather than artificially suppressed.

For tracks 64 and 71, which cover the epicentral area of the M6.4 and M7.1 July 4–5, 2019 Ridgecrest, California earthquake sequence (e.g., Xu et al., 2020) and are strongly affected by coseismic displacements, a step function fit at the epoch corresponding to the earthquakes in each time series is added to account for the combined

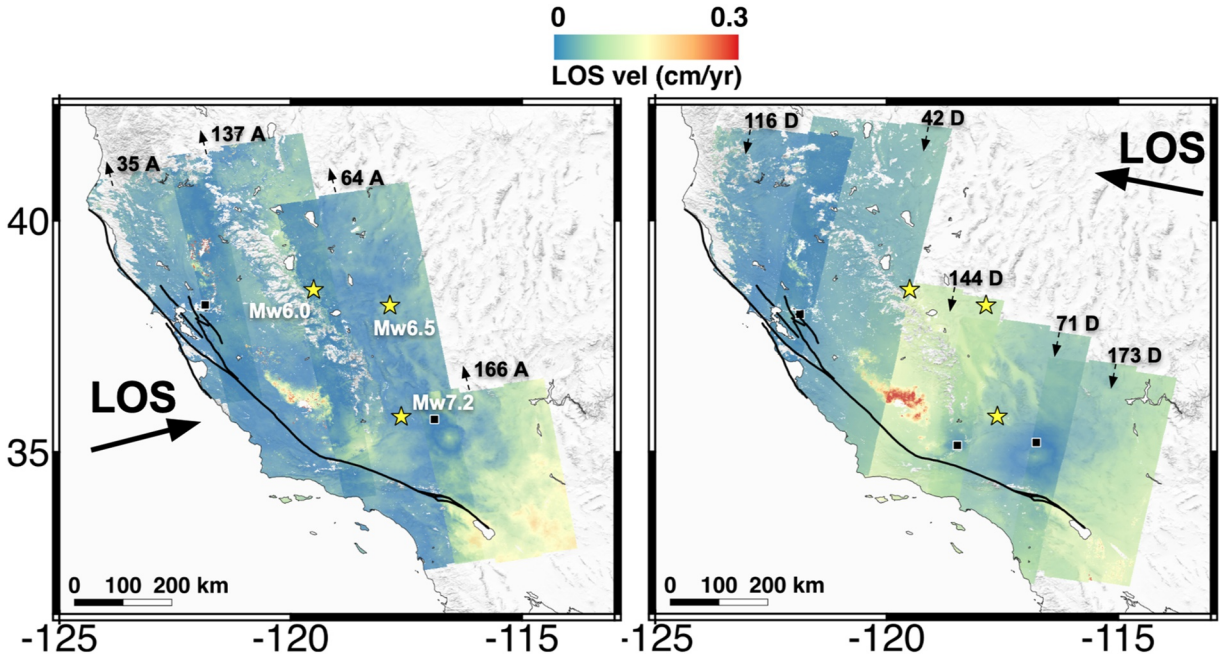


Figure 2. Maps of one-sigma LOS velocity uncertainty for ascending (a) and descending (b) tracks, derived as the standard deviation of 1000 bootstrap fits per pixel. Uncertainties are lowest over arid basins and urban areas with high correlation (see Figure 8), and elevated over forested and high-relief terrains, permanent water bodies, and along strong displacement gradients (e.g., rims of Central Valley subsidence bowls, creeping fault traces, and near-field coseismic/postseismic zones). Range-dependent geometry and reference-point placement also have some influence, with far-range regions and areas away from the reference point generally exhibiting larger values. Weather-model tropospheric corrections reduced the expected broad evening–morning differences, yielding comparable ascending/descending magnitudes. Symbols and basemap sources as in Figure 1.

displacements of the events and to more accurately constrain the secular velocity field. Similar offsets are estimated for the M6.5 15 May 2020 Monte Cristo, Nevada and M6.0 8 July 2021 Antelope Valley, California earthquakes in the relevant tracks. In addition, we apply additional corrections within MintPy to mitigate other sources of potential error and bias in our data, including DEM errors, which can be estimated by looking for phase biases that correlate with perpendicular baseline (e.g., Ferretti et al., 2001), and phase unwrapping errors, which are corrected using a phase-bridging approach that connects reliable regions of each interferogram and estimates integer-cycle offsets between them under the assumption of smooth phase gradients (Chen & Zebker, 2002; Yunjun et al., 2019).

A detailed visualization of our processing architecture along with an itemized breakdown of all primary MintPy software runtime parameters is provided in the Figure S4 and Table S1 in Supporting Information S1. The complete set of track-specific configuration files used to execute these inversions can be directly accessed via the Zenodo repository link listed in the Open Research.

2.3. Uncertainty Analysis

A commonly used method for estimating uncertainty in InSAR velocities is to calculate the formal uncertainty in the linear fit to the time series. This approach has fallen out of favor in analysis of GNSS velocities as it can dramatically underestimate the true uncertainties involved—because the displacement at each epoch depends on the previous epoch, errors in position are not independent, and without explicitly considering the correlated nature of these errors, the estimated uncertainties become vanishingly small for long GNSS time series, which may span a decade or longer (Langbein & Johnson, 1997; Mao et al., 1999; Zhang et al., 1997). The lengths of contemporary InSAR time series are approaching a decade, and formal uncertainties in velocity fits are starting to show similar issues to the GNSS cases described above.

To obtain more realistic estimates of velocity uncertainty, we apply a non-parametric resampling technique known as bootstrapping (Efron & Tibshirani, 1986; see Figure 2), following the implementation by Bekaert, Hooper, et al. (2015) and Bekaert, Walters, et al. (2015). This method does not rely on assumptions about the

23335084, 2026, 8, Downloaded from https://agupubs.onlinelibrary.wiley.com/doi/10.1029/2026EA005214, Wiley Online Library on [29/09/2026]. See the Terms and Conditions (https://onlinelibrary.wiley.com/terms-and-conditions) on Wiley Online Library for rules of use; OA articles are governed by the applicable Creative Commons License

23335084, 2026, 8, Downloaded from https://agupubs.onlinelibrary.wiley.com/doi/10.1029/2026EA005214, Wiley Online Library on [29/09/2026]. See the Terms and Conditions (https://onlinelibrary.wiley.com/terms-and-conditions) on Wiley Online Library for rules of use; OA articles are governed by the applicable Creative Commons License

underlying error distribution and is particularly well-suited for complex data sets with temporal correlations, such as InSAR time series. In our implementation, each time series is resampled 1000 times by randomly drawing observations with replacements from the original data set. Each bootstrap sample preserves the original data set sample size, but individual time steps may be repeated or omitted, introducing variability that reflects the statistical uncertainty in the data. We perform a linear regression for each bootstrap sample to estimate the displacement rate (i.e., velocity), producing a distribution of 1000 velocity estimates. The standard deviation of this distribution is then used to quantify the uncertainty in the estimated velocity field for each pixel in the data set.

This process introduces variability across the resampled data sets and estimated velocity that reflects the statistical uncertainty of the original data set. This has the effect of implicitly modeling the influence of temporal correlations (which are common in InSAR data due to atmospheric or orbital effects), even though no explicit correlation structure is imposed. In doing so, bootstrapping allows us to explore the sensitivity of the velocity estimate to the specific time sampling and noise characteristics of the data. Overall, this approach provides a robust, data-driven estimate of velocity uncertainty, accommodating irregularities and temporal dependencies in the observations without requiring parametric assumptions about the distribution or correlation of the errors.

2.4. Accuracy Assessment

While our bootstrapping approach allows us to assess uncertainties, and thus the *precision* of our processed velocities, in order to assess the *accuracy* of our processed data, we must validate them against independent data. For this, we follow the established methodology and tools used to verify the NISAR Solid Earth Science team Level-2 mission requirements (Simons et al., 2021) and the accuracy validation of NASA's Observational Products for End-Users from Remote Sensing Analysis (OPERA) project's Surface Displacement (DISP) products (NASA/JPL/OPERA, 2025) and conduct validation analyses for our InSAR velocities to assess pixel stability and reliability in both space and time.

We use GNSS time-series data from the Nevada Geodetic Laboratory at the University of Nevada, Reno (Blewitt et al., 2018) as independent displacement measurements for validation. We project these data into the radar LOS direction and use them to estimate velocities over the same time span and using the same parametric time series models that we fit to our InSAR time series as outlined in Section 2.2. Only GNSS stations that cover the full analysis period (Table 1) and are free of uncorrected artifacts or instrument changes are included.

For each InSAR track, we initially inspect overlapping GNSS time series to identify a stable reference site. Referencing all InSAR velocities to a single site can introduce bias due to imprecise registration between InSAR and GNSS data sets. To mitigate this, we compute differences in relative velocity between pairs of GNSS stations and their corresponding InSAR estimates—referred to as the "double-difference" method. We then compute the root-mean-square error (RMSE) of these residuals to determine whether the InSAR data meet validation criteria. Weiss et al. (2020) provide an example of large-scale validation by combining Sentinel-1 InSAR with GNSS across Anatolia, achieving high-resolution strain rate fields; their work illustrates the effectiveness of double-difference comparisons in quantifying uncertainty and guiding confidence thresholds for InSAR-derived velocities. We also assess the agreement between each GNSS time-series and spatially collocated InSAR time-series pixels by quantifying the average RMSE across time and through basic qualitative inspection.

All validation tools were implemented in a Jupyter Notebook environment, building on ARIA-tools and MintPy workflows originally developed by the authors and collaborators through earlier efforts, and later adopted and extended within the publicly available NISAR Solid Earth validation framework (NISAR ATBD Notebooks, 2024) following community engagement and software demonstration under EarthScope Consortium—formerly the University NAVSTAR Consortium (UNAVCO)—sponsored courses. Requirements were guided by the NISAR Algorithm Theoretical Basis Document review (NISAR ATBD Review, 2024), which captures the methods and uncertainty criteria outlined above. Complete, end-to-end validation workflows for each track are archived and made available to the reader through dedicated Jupyter Notebooks (e.g., see Figure S1 in Supporting Information S1 for an example).

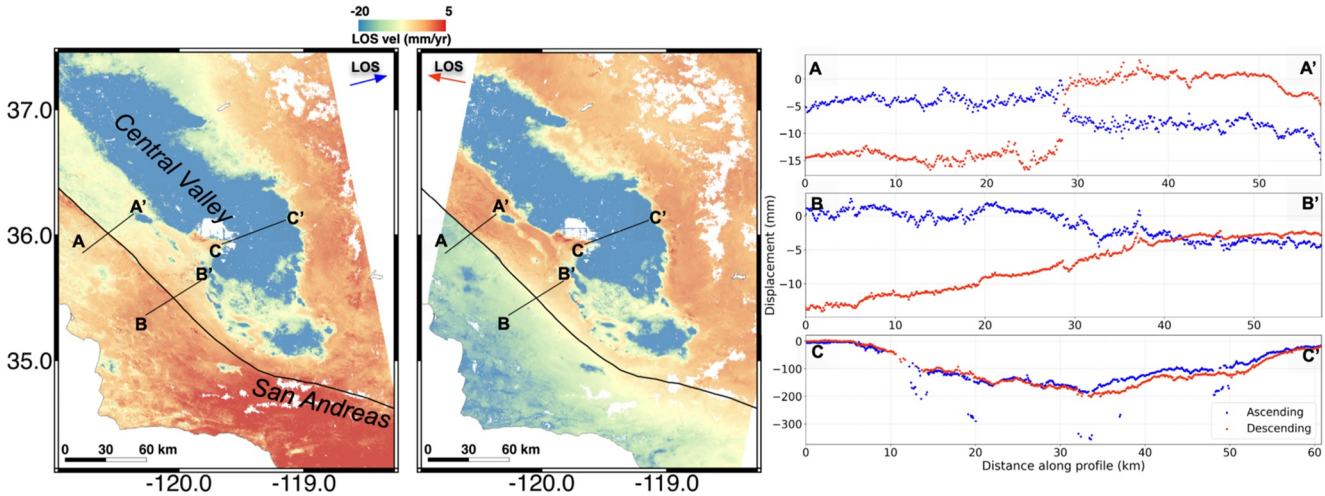


Figure 3. (Left) LOS surface velocities across Central California derived from ascending and descending Sentinel-1 tracks 137 and 144, respectively. Velocities are referenced to a single GNSS station (black square) for each track. (Right) Cross-sectional velocity profiles along the transects denoted on the maps. Profile A–A′, located along the creeping segment of the San Andreas Fault, exhibits a sharp velocity discontinuity coincident with the fault trace. Profile B–B′, positioned on a locked segment of the San Andreas, displays the characteristic arctangent-shaped velocity gradient associated with elastic strain accumulation. The reversal in velocity offset between the ascending and descending geometries reflects predominantly horizontal fault-parallel motion. Profile C–C′ crosses a region of maximum subsidence rate within the Central Valley, with both the ascending and descending data showing rapid motion away from the satellite (note the change in the displacement scale compared to A–A′ and B–B′).

3. Results

3.1. Data Selection

We show results of our velocity analyses in Figure 1, with corresponding uncertainty estimates in Figure 2. Each is plotted with their associated reference points which were selected in areas of high correlation and low displacement. In general, the major velocity signals are larger than their corresponding uncertainties, with the largest uncertainties (up to 3 mm/yr) in areas of the largest velocity signals (which exceed 10 cm/yr in magnitude), and more typical uncertainties of 1 mm/yr or less over the majority of the data set, which we will discuss in more detail in Section 3.2 below. Velocities are expressed using a convention in which motion toward the satellite is positive and motion away from the satellite is negative, consistent with a ground-displacement (negative range-change) convention. Data coverage is excellent over the majority of the area of interest, with most of the signal loss due to decorrelation (<10% of the total valid land area; see Table 1) occurring over bodies of surface water, the coastal forests of NW California and the steep mountain terrain of the high Sierra Nevada, areas in which InSAR with C-band radar is likely to be challenging.

The deformation field across the majority of the tracks is dominated by two major deformation sources. The larger in amplitude of these two is centered on the agricultural areas of the Central Valley in California (also known as the Great Valley, and in its southern portion, the San Joaquin Valley), and has a sense of motion that is consistently negative, hence related to subsidence, most likely due to ongoing extraction of groundwater and associated deformation that has continued for decades (e.g., Carlson et al., 2020; Govorcin et al., 2025; Jones et al., 2022; Miller et al., 2020; Neely et al., 2021; Poland et al., 1975). This subsidence occurred at rates exceeding 10 cm/yr in places during the period spanned by our data (Figure 3).

The second major feature of the deformation pattern is a tectonic signal associated with the major plate boundary faults of the San Andreas Fault system (Figures 3–5). This feature appears as a positive to negative gradient (from west to east) over a length scale of ∼100 km in ascending track data, and a negative to positive gradient in descending track data over a similar length scale. The reversal in the sense of the gradient with the change in viewing geometry from ascending to descending tracks indicates that this deformation has a significant east-west component, in this case, consistent with right-lateral shear across the San Andreas Fault and other plate boundary-parallel faults. While this shear is expressed along most of the plate boundary as a gradient, indicating that faults are locked at the surface and accumulating elastic strain, in places—notably the 200 km-long central 'creeping segment' of the San Andreas, along with segments of the Maacama, Hayward and Calaveras faults in the plate

23335084, 2026, 8, Downloaded from https://agupubs.onlinelibrary.wiley.com/doi/10.1029/2026EA005214, Wiley Online Library on [29/09/2026]. See the Terms and Conditions (https://onlinelibrary.wiley.com/terms-and-conditions) on Wiley Online Library for rules of use; OA articles are governed by the applicable Creative Commons License

10.1029/2026EA005214

23335084, 2026, 8, Downloaded from https://agupubs.onlinelibrary.wiley.com/doi/10.1029/2026EA005214, Wiley Online Library on [29/09/2026]. See the Terms and Conditions (https://onlinelibrary.wiley.com/terms-and-conditions) on Wiley Online Library for rules of use; OA articles are governed by the applicable Creative Commons License

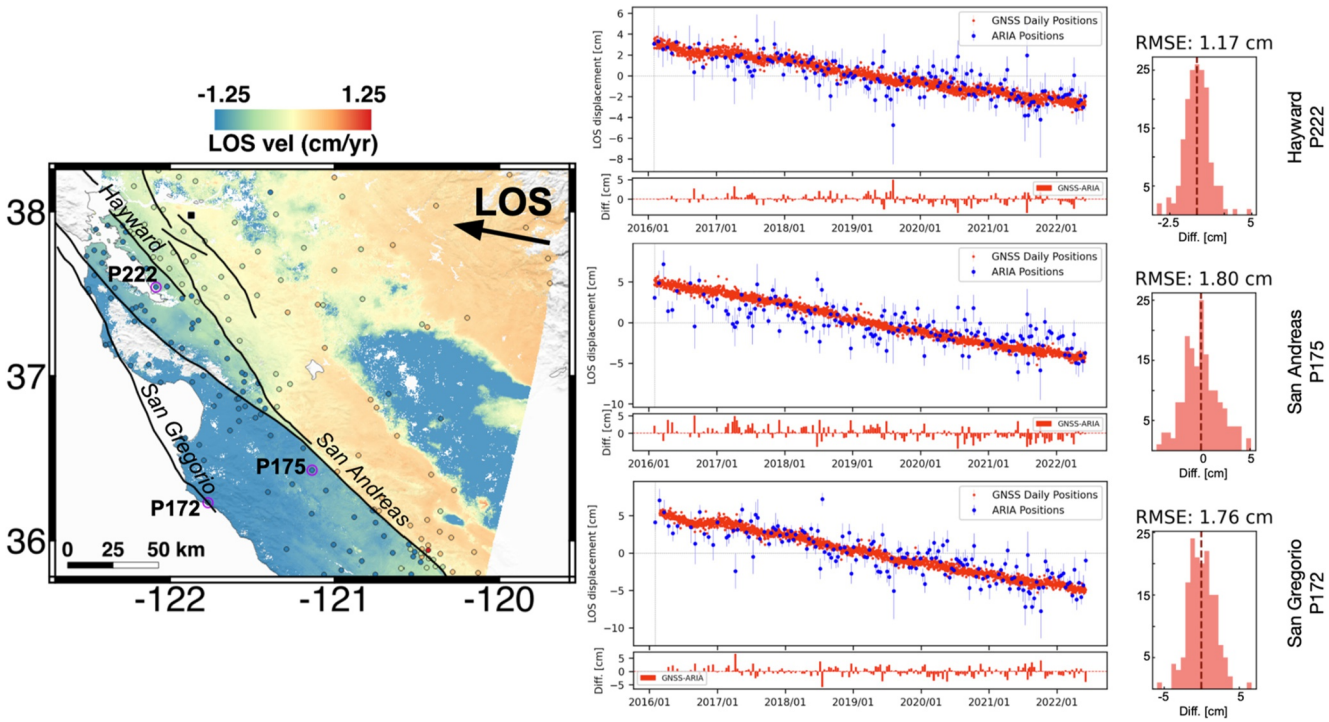


Figure 4. (Left) LOS surface velocity across the Bay Area captured in descending track 42. (Right) InSAR-GNSS comparison scatter plots of collocated time-series histories, with InSAR data denoted by blue and GNSS in red, with GNSS station P248 serving as the reference point (see Table 1). Error-bars for InSAR represent the residual between each date and the best-fit velocity. Error-bars for GNSS representing the standard error of each observation are roughly the size of the markers and have been omitted. At the bottom of each InSAR-GNSS comparison scatter plot are histograms capturing the difference between InSAR and GNSS at each observation point, and to the left are histograms aggregating these differences across all time and titled with the computed RMSE. Associated fault and collocated GNSS station names denoted to the right of each plot. InSAR is consistent with GNSS in tracking overall fault creep across each distinct segment, though the larger scatter of individual InSAR observations translates to a ∼1–2 cm RMSE in the overall InSAR and GNSS difference.

boundary zone—the change in velocity is abrupt and localized along the faults' surface traces, indicating that the faults are creeping at the surface, as inferred by other authors (e.g., Jolivet et al., 2015; Ryder & Bürgmann, 2008).

At smaller spatial scales, the pattern of InSAR deformation velocities reveals a rich variety of deformation sources. One area where these are particularly apparent is the greater Los Angeles Basin (Figure 5, Figure S2 in Supporting Information S1), where deformation is strongly influenced by groundwater withdrawal and hydrocarbon extraction (e.g., Argus et al., 2005).

Profiles extracted from the velocity fields highlight several characteristic deformation patterns. Across the Santa Ana Basin (profile A–A′), ascending and descending LOS velocities show the same pattern. This consistency indicates deformation dominated by vertical motion, as vertical displacement projects with the same pattern and relative motion into the two radar viewing geometries. A similar spatial pattern was documented by Bawden et al. (2001), who analyzed ERS interferograms spanning ∼October 1997 to September 1999 and observed seasonal uplift and subsidence cycles associated with groundwater storage variations. Our Sentinel-1 observations (∼2014–2023) instead capture the longer-term secular component of this deformation field. Because side-looking radar observations acquired along near-polar trajectories are fundamentally insensitive to north-south horizontal velocity components, this multi-geometry interpretation explicitly assumes that vertical and east-west variations constitute the primary drivers of the observed LOS signal.

A second prominent signal is observed over the Wilmington oil field near Long Beach (profile B–B′), where both ascending and descending velocities show a strong, localized peak of ∼10 mm/yr near the center of the profile. The coincidence of this signal in both viewing geometries suggests deformation dominated by vertical motion associated with hydrocarbon extraction and injection, but some offset in this peak between the two viewing geometries indicates some East-West motion. Episodic subsidence of the Wilmington field was also documented by Bawden et al. (2001), indicating that anthropogenic deformation in this region has persisted for decades.

10.1029/2026EA005214

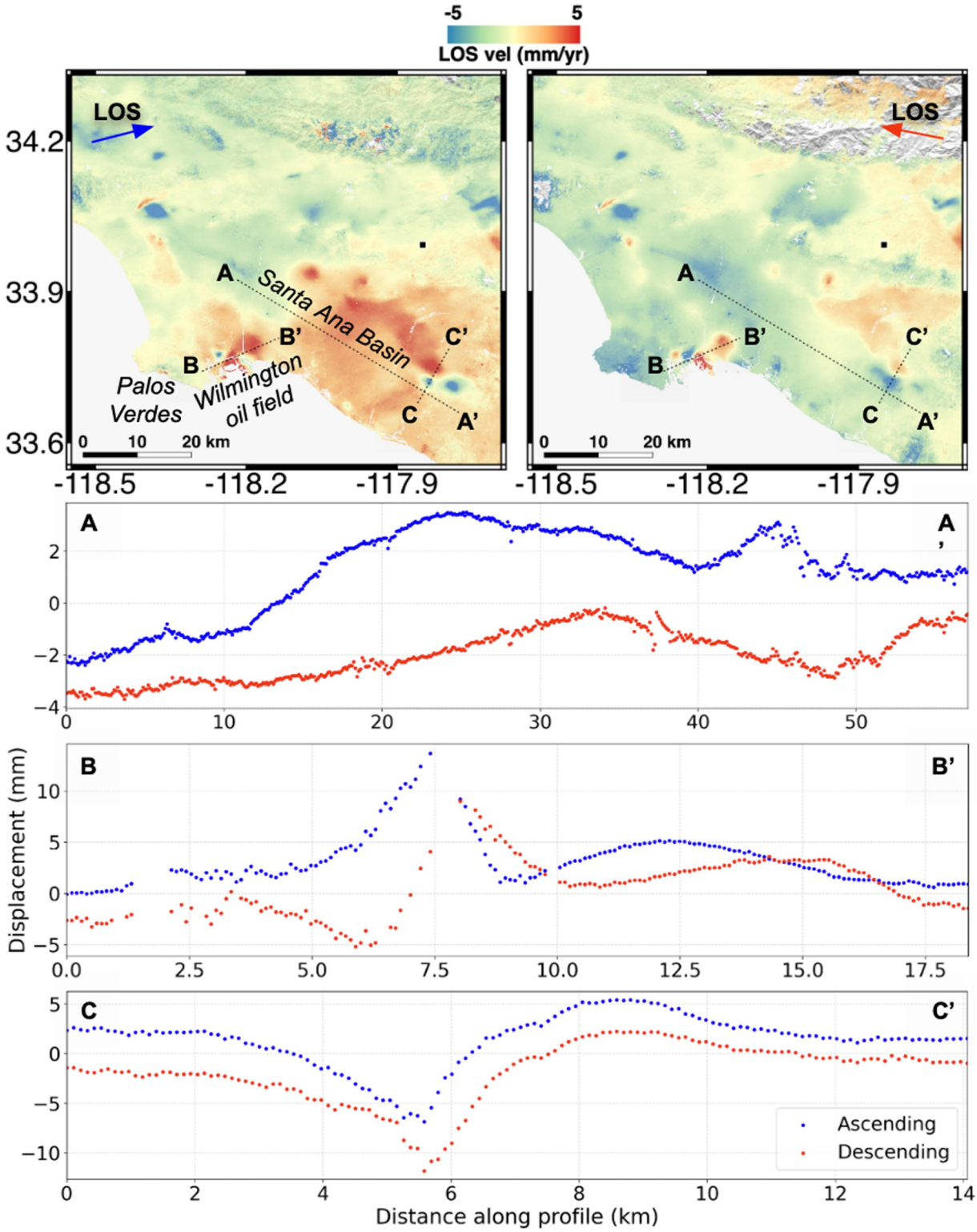


Figure 5.

23335084, 2026, 8, Downloaded from https://agupubs.onlinelibrary.wiley.com/doi/10.1029/2026EA005214, Wiley Online Library on [29/09/2026]. See the Terms and Conditions (https://onlinelibrary.wiley.com/terms-and-conditions) on Wiley Online Library for rules of use; OA articles are governed by the applicable Creative Commons License

23335084, 2026, 8, Downloaded from https://agupubs.onlinelibrary.wiley.com/doi/10.1029/2026EA005214, Wiley Online Library on [29/09/2026]. See the Terms and Conditions (https://onlinelibrary.wiley.com/terms-and-conditions) on Wiley Online Library for rules of use; OA articles are governed by the applicable Creative Commons License

In the southern Santa Ana Basin (profile C–C′), ascending and descending profiles closely mirror one another, with peak LOS subsidence of approximately −5 to −10 mm/yr near the basin center and relative uplift toward the basin margins. This pattern is consistent with groundwater-related deformation documented in previous InSAR and geodetic studies of the region based on data from the ERS and Envisat missions (e.g., Argus et al., 2005; Bawden et al., 2001; Lanari et al., 2004; Riel et al., 2018).

Overall, the similarity between ascending and descending signals along these profiles indicates that most of the LOS velocity in these areas reflects vertical deformation, with any differences likely representing a smaller radial component of horizontal motion projecting into the east–west direction. Their consistency with earlier studies based on data from ERS and Envisat indicates that groundwater-driven subsidence in the Santa Ana Basin and deformation associated with hydrocarbon extraction in the Wilmington oil field have persisted for decades. While those earlier observations captured seasonal deformation cycles over shorter intervals, the Sentinel-1 time series analyzed here provides a longer-term view of the secular deformation field across the basin.

We can also identify signatures of landsliding in Figure 5, where reversals in sign between the ascending and descending geometries indicate primarily horizontal motion—for example, the Portuguese Bend landslide near Palos Verdes, whose creeping movement has caused considerable infrastructure and property damage (Li et al., 2024).

3.2. Uncertainties and the Effect of Troposphere Corrections

The pattern of uncertainties across our ascending and descending tracks (Figure 2) reveals several main features. First, there are three main factors that we consider as major contributors to uncertainty: (a) residual tropospheric noise in the individual interferograms; (b) the quality (interferometric correlation) of the data; and (c) the geometric factors associated with the time-series configuration, such as reference-point placement and radar look-angle geometry, which affect the projection of motion into the line of sight and the spatial distribution of uncertainty (see Section 4.1.3).

InSAR-GNSS comparison scatter plots of collocated LOS rates before and after applying tropospheric corrections to the InSAR data demonstrate a consistent reduction in scatter (Figure 6). Additionally by visual inspection, we can see that the applied tropospheric corrections have some effect on the estimated velocities. Qualitatively, the corrected velocities look to have a "flatter" overall appearance, which is particularly noticeable in the north and eastern portions of each track, away from the San Andreas system. This is particularly apparent in the ascending track data, which are all acquired in the early evening (around 6.05 p.m. PST), a time of more elevated and variable tropospheric activity (compared with the descending track data, acquired around 6.15 a.m. PST) due to solar heating of the atmosphere (Stephens et al., 2020; Tomic, 2011), suggesting that there may be a larger contribution of tropospheric noise to remove from those data. This can also be determined from the velocity uncertainties (Figure 2) which show the uncertainties for the ascending data were larger than those for the descending data when uncorrected, but at a similar level when corrected for troposphere noise.

3.3. InSAR-GNSS Time Series Comparisons

To validate our InSAR analysis, we can make use of data from continuous GNSS stations, which provide independent estimates of surface displacement and velocity. Our validation approach is a two-step process: first, we compare differential time series for both InSAR and GNSS between pairs of GNSS station locations; second, we compare the velocities that are derived from those time series over the same time period. While the intent of this study is to focus on the estimation and characteristics of the InSAR velocities, we recognize that their reliability depends on the quality and temporal behavior of the underlying time series. In particular, our velocity estimates assume approximately linear deformation over the analysis period—a simplifying assumption that we evaluate

Figure 5. (Top) LOS surface velocities across the greater Los Angeles Basin derived from Sentinel-1 ascending track 64 and descending track 71. (Bottom) Cross-sectional velocity profiles extracted along the transects denoted on the maps. Profile A–A′ spans the Santa Ana Basin, B–B′ crosses the Wilmington oil field near Long Beach, and C–C′ traverses the southern Santa Ana Basin near groundwater wells examined by Bawden et al. (2001). Opposite-sign velocities between ascending and descending geometries across the Santa Ana Basin indicate deformation dominated by vertical motion, while localized signals near Wilmington highlight anthropogenic deformation associated with hydrocarbon extraction. These observations are broadly consistent with earlier InSAR studies of deformation in the Los Angeles Basin (e.g., Bawden et al., 2001).

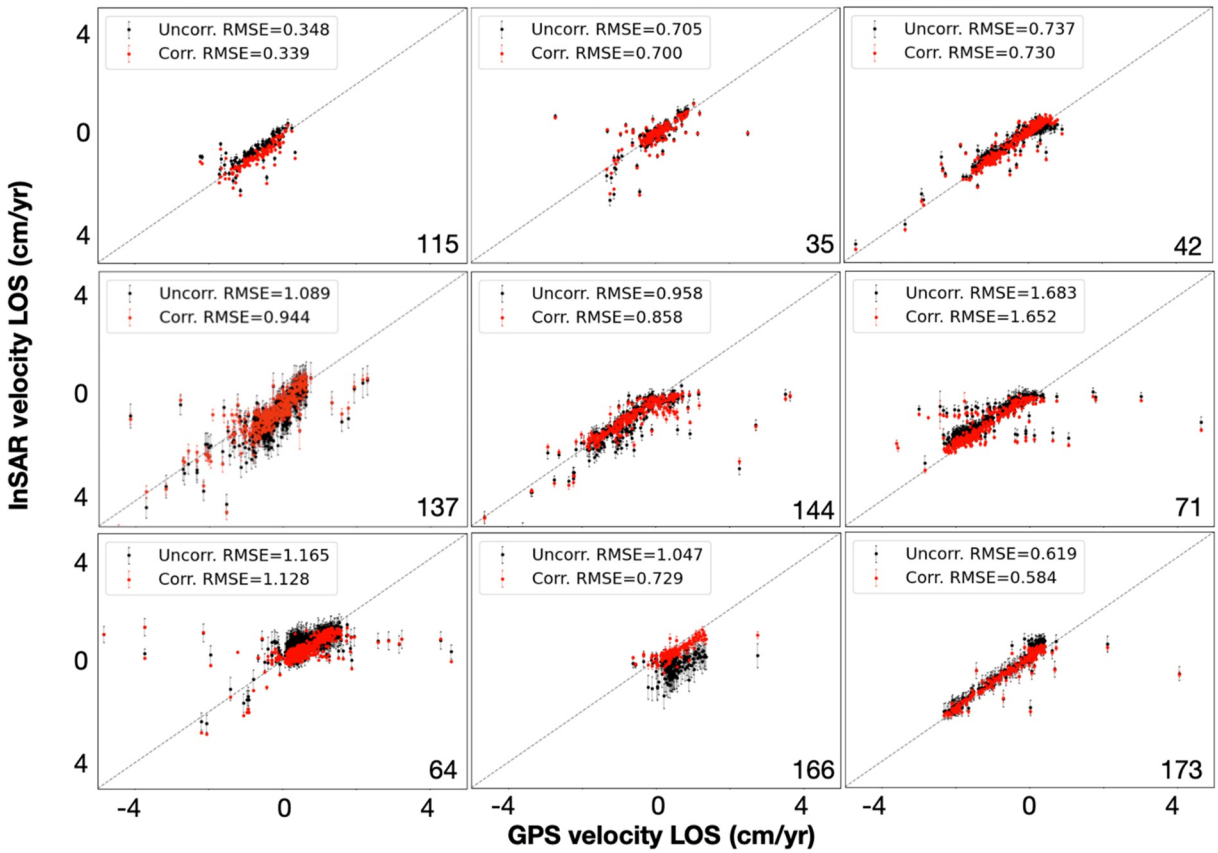


Figure 6. InSAR-GNSS comparison scatter plots of collocated LOS rates before (black) and after (red) tropospheric corrections, reported in centimeters per year (cm/yr) to properly scale the high-magnitude subsidence signals captured across the statewide GNSS array. Error-bars correspond to 1-sigma. Black 1:1 lines are shown for comparison. We find closer agreement between GNSS and the corrected InSAR velocities with consistent reduction in estimated RMSE (reported in each respective subplot legend). Rates outside of the ±5 cm/yr range have been excluded in the visualization here, but kept when computing RMSE; we suspect that disagreements at these larger deformation rates are due to aliasing of the InSAR signal since they are restricted to rapidly deforming regions such as the Central Valley.

later in Section 4.2, where we examine deviations from linear trends and their implications for uncertainty and physical interpretation.

As our InSAR displacements and velocities are relative measurements, not formally tied to a reference frame, we must compare them to relative motions between pairs of GNSS stations: a reference station that is collocated with the reference point for our InSAR data sets, and a series of other GNSS stations covered by the InSAR track being assessed, taken from the Network of the Americas (NOTA), operated by EarthScope. InSAR measures deformation velocities mapped into the LOS direction, and so to produce a comparable measure of displacement from GNSS data, we project the GNSS displacements, epoch by epoch, into the LOS of each track (Figure 1) for the same time period. Taking each InSAR data set in turn, we first project all three components of the GNSS time series at each station covered by that track into the radar LOS. Then we difference these GNSS LOS time series between each pair of stations to produce differential GNSS LOS time series. We then compare these with the differenced InSAR LOS time series for the same pairs of locations (Figure S1 in Supporting Information S1).

Examples of time series comparisons are shown in Figure 4. Qualitatively, the trends of the time series align between GNSS and InSAR, although there is significantly greater scatter in the InSAR with RMSE values ranging from ∼1 to 2 cm here.

3.4. InSAR-GNSS Velocity Comparisons

To assess the overall quality of each InSAR velocity data set, we compare, track by track, velocities of our InSAR data with GNSS velocities projected into the radar LOS for that track. Both sets of velocities are effectively differential velocities—the InSAR with respect to the chosen reference point for that track (Figure 1, Table 1),

23335084, 2026, 8, Downloaded from https://agupubs.onlinelibrary.wiley.com/doi/10.1029/2026EA005214, Wiley Online Library on [29/09/2026]. See the Terms and Conditions (https://onlinelibrary.wiley.com/terms-and-conditions) on Wiley Online Library for rules of use; OA articles are governed by the applicable Creative Commons License

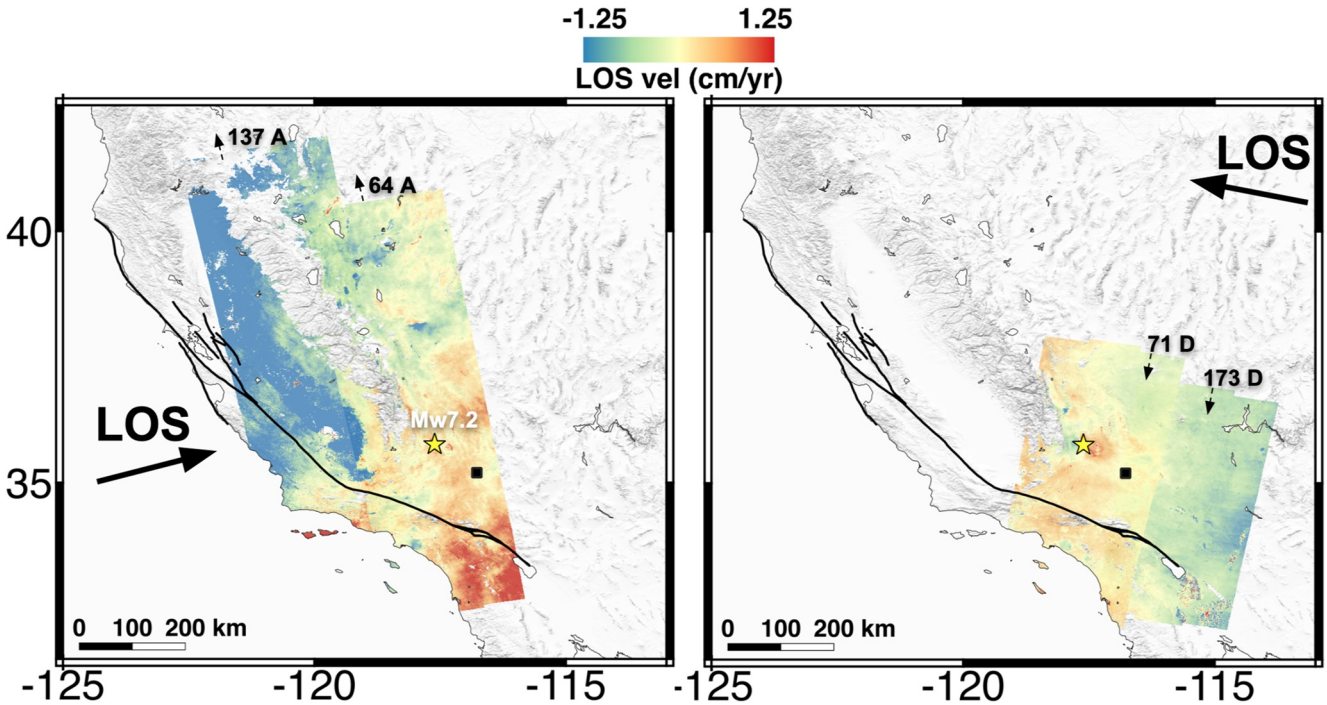


Figure 7. Post- and pre-Ridgecrest earthquake difference in LOS surface velocities for ascending and descending tracks, respectively. Velocities are referenced to a single GNSS station (black square) for each track. Positive motions indicate motion of the ground toward the satellite, and vice-versa. The largest divergences in the velocity fields occur in the epicentral area, as well as across the rapidly deforming Central Valley region where the subsidence rate has increased in the drought years immediately succeeding the Ridgecrest earthquake (Carlson et al., 2020; Neely et al., 2021).

which is collocated with a GNSS station; and the GNSS with respect to the velocity of the station at the InSAR reference point. This comparison is made at all of the GNSS stations covered by the InSAR data from each track; as in the cases of the time series comparisons mentioned above, these GNSS stations are drawn from the NOTA.

We show this comparison as a series of scatterplots in Figure 6, plotting the LOS-projected GNSS velocities on the horizontal axis and the InSAR velocities on the vertical axis. Both troposphere-corrected and uncorrected InSAR velocities are plotted. Visually, the velocities that have been corrected for the troposphere appear closer to the 1:1 trendline in almost all cases, implying a close agreement between those data and the GNSS velocities. In contrast, the uncorrected velocities appear systematically offset from the line, either above or below it, by up to ∼1 mm/yr. This is in line with our expectations—GNSS data are routinely corrected for troposphere delay during processing, and so we would expect that InSAR data that are also corrected for the effect of the troposphere should agree better with them.

Quantitatively, we find an improved agreement for the troposphere-corrected InSAR velocities for all tracks analyzed, based on a reduction in the root-mean-squared (RMS) difference between the InSAR and GNSS velocities. Residual long-wavelength spatial ramps that persist post-correction are attributed to unmodeled signals, such as dispersive ionospheric phase delays, solid Earth tide (SET) strains, or tectonic plate rotations, which were not explicitly estimated or subtracted within this baseline workflow. We note that some of the largest discrepancies between the InSAR and GNSS velocities are seen at some of the fastest moving sites, suggesting that the InSAR may be less accurate at estimating large velocities, potentially due to aliasing of the signal during intervals of large displacement, which subsequently induces localized phase unwrapping errors. These high magnitude outliers are concentrated over high gradient agricultural pumping basins within the Central Valley, where localized groundwater extraction drives subsidence velocities exceeding 10 cm/yr. Because Track 137 spans the entire longitudinal extent of the Central Valley and encompasses a particularly dense network of collocated ground stations, cross-validation with GNSS yields a wide displacement profile along the 1:1 axis (Figure 6). Units of centimeters per year (cm/yr) are intentionally maintained across these broad validation scatterplots to properly scale these rapid anthropogenic signals without saturating the axes.

23335084, 2026, 8, Downloaded from https://agupubs.onlinelibrary.wiley.com/doi/10.1029/2026EA005214, Wiley Online Library on [29/09/2026]. See the Terms and Conditions (https://onlinelibrary.wiley.com/terms-and-conditions) on Wiley Online Library for rules of use; OA articles are governed by the applicable Creative Commons License

23335084, 2026, 8, Downloaded from https://agupubs.onlinelibrary.wiley.com/doi/10.1029/2026EA005214, Wiley Online Library on [29/09/2026]. See the Terms and Conditions (https://onlinelibrary.wiley.com/terms-and-conditions) on Wiley Online Library for rules of use; OA articles are governed by the applicable Creative Commons License

4. Discussion

4.1. Limitations in Data Coverage and Data Quality

The coverage of our data (i.e., the area covered by estimated velocities) varies regionally, and is largely a reflection of the amount of decorrelation in the data. As described above, decorrelation can hamper unwrapping of the interferometric phase, resulting in the masking out of such areas, with concomitant loss of spatial coverage. Likewise, the quality of our data (i.e., the strength of deformation signals compared to noise) is also affected by phase noise introduced by decorrelation, but also affected by factors such as residual tropospheric noise and the reference point location. We will explore the different conditions that affect data coverage and data quality, and their spatial variations, below.

4.1.1. Decorrelation

Decorrelation noise arises when the radar scattering properties of the ground change between acquisitions, preventing cancellation of its interferometric phase (Fielding et al., 2005; Rosen et al., 2000; Wei & Sandwell, 2010; Zebker & Villasenor, 1992). Major sources include geometric, volume, and temporal decorrelation, associated with viewing geometry, vegetation structure, and surface change, respectively.

In addition, strong spatial gradients of displacement can reduce correlation when the differential phase between adjacent pixels approaches a significant fraction of the radar wavelength over the repeat interval. This effect is observed along steep interseismic strain gradients near locked faults, across transitions at creeping fault traces, within subsidence bowls, and most prominently in near-field coseismic and postseismic regions. In these areas, correlation loss and unwrapping errors often align with displacement gradients, producing characteristic artifacts that require conservative masking or localized modeling (Fielding et al., 2005; Xu et al., 2020).

To minimize decorrelation, a range of earlier studies employing InSAR data to solve for interseismic deformation rates have highlighted the importance of using interferogram pairs with short spatial and temporal baselines (e.g., Biggs et al., 2007; Fialko, 2006; Wright et al., 2001). However, given the limited spatial baseline variation for Sentinel-1 during the timespan of our analysis, with the satellites' positions being maintained within a tight 250 m orbital tube, we do not take special precautions to avoid geometric decorrelation. We mitigate the problem of temporal decorrelation by exploiting the regular and consistent acquisitions of Sentinel-1 data (every 12 days in California). As discussed in Section 2.1, we limit ourselves to the 3 nearest neighbor pairs (temporal baselines up to 36 days) and add annual pairs to bridge decorrelated winter periods through late spring/early fall. The severity of volumetric decorrelation, on the other hand, depends on the radar wavelength. The C-band radar on Sentinel-1 is sensitive to objects with length scales of a fraction of a wavelength—10 mm or so—the scale of small branches or leaves. This fine sensitivity means that random structural changes within the canopy architecture caused by vegetation growth or seasonal decay result in rapid temporal decorrelation at shorter wavelengths (Zebker & Villasenor, 1992). The significantly longer, 4 times longer, L-band radar wavelengths of the ALOS-2 and NISAR missions would only be sensitive, in turn, to larger objects such as large branches or tree trunks, which are fewer in number and more stable. Empirical comparisons over vegetated regions in California confirm that these longer wavelengths propagate through the outer canopy to interact with stable woody structures, yielding significantly higher coherence over multiyear intervals than C-band systems (Wei & Sandwell, 2010). However, data from those satellites were not available for this study.

We observe significant spatial variation in correlation across California. The correlation metric used within the ARIA_S1_GUNW products is the phase sigma correlation, which estimates correlation from the phase variance, calculated from a moving window of detrended data (e.g., Rodriguez & Martin, 1992; Rosen et al., 2000). With this metric, values near 0.75 are considered high and those near 0.5 moderate, while values below ~0.3 are regarded as low and the associated interferometric phase unreliable. High correlation is typically associated with stable surfaces that produce consistent radar returns, such as the arid desert environments found to the east of the Sierra Nevada and the Transverse Ranges and in urban areas across the state, whereas low correlation arises in regions with dense vegetation, persistent surface water, or rapid deformation relative to the SAR satellite sampling interval (e.g., Zebker & Villasenor, 1992). Across California, the computed mean spatial correlation (Figure 8) is lowest (<0.3) over permanent water bodies, heavily vegetated areas, steep mountain terrain, and zones of peak subsidence in the Central Valley. These pixels are captured and excluded using our velocity map masks, which combine zero-connected component fields from SNAPHU with permanent water body maps (see

10.1029/2026EA005214

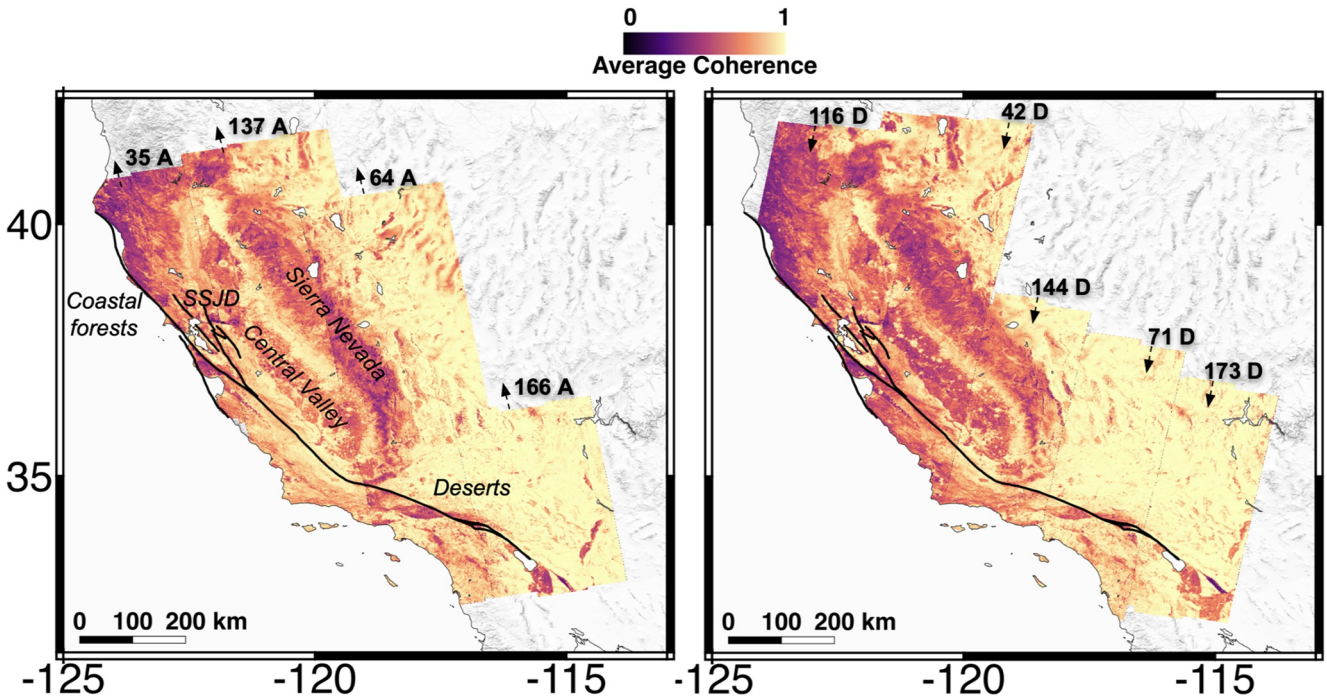


Figure 8. Average spatial correlation for ascending and descending passes, respectively. Correlation is highest over arid deserts and urban surfaces, and lowest over forests, steep topography, permanent water, and high-gradient subsidence rims (see Figure 1). Specifically there are correlation lows across the Northern California coastal forests, Central Valley subsidence bowl, along the Sierra Nevada, and the Sacramento-San Joaquin Delta (SSJD on left). Desert-dominated tracks to the south and east maintain uniformly high correlation with minor reductions over playas, irrigated fields, and Salton Sea margins.

Section 2.1). Outside of these regions, which represent less than 10% of the study area (Table 1), spatial correlation is broadly moderate-to-high, with the highest values observed in the arid, desert regions of eastern California. Lower correlation across northern California can be attributed to denser vegetation (including forests), reflecting a relatively wetter climate.

The spatial patterns outlined above manifest consistently by track (Figure 8) and align with the valid-pixel fractions summarized in Table 1. Tracks that transect persistently vegetated or mixed land-use terrains show the largest masked fractions/lowest valid-pixel percentages. For example, track 35 A (centered over the Coast Ranges/Bay Area) degrades over the Sonoma–Mendocino forests, the Marin/Sonoma coast, and Sacramento–San Joaquin Delta wetlands, while 115 D similarly loses correlation across North Coast forests and over the high-gradient rims of Central Valley subsidence bowls. Both tracks have the lowest valid-pixel fractions of 80.38% and 81.17%, respectively. Track 137 A exhibits minima along the Sierra crest and foothill forests with localized drops where agricultural subsidence is strongest; 42 D and 144 D likewise show decreased correlation across the San Joaquin basin, Delta wetlands, and steep Sierra foothills, improving southward into interior basins. Conversely, desert-dominated swaths—71 D (Mojave), 166 A (Mojave/Colorado), 173 D (eastern deserts), and much of 64 A (Owens/Death Valley)—retain very high valid fractions (96.62%, 98.11%, 98.33%), with only localized losses over playas, ephemeral water bodies, and intensively irrigated fields (e.g., Imperial Valley, Salton Sea margins). Tracks 137 A and 144 D, crossing the Central Valley and southern Sierra foothills, have intermediate values (88.52%, 89.28%), and are associated with agricultural subsidence bowls and forested slopes. In several of these tracks, correlation losses align with strong spatial gradients of displacement (e.g., subsidence rims and creeping fault zones), underscoring the role of decorrelation and phase aliasing in addition to the geometric, volumetric, and temporal decorrelation sources noted above. In such regions, rapid phase changes can exceed the sampling capability of the sensor, leading to missed phase cycles and underestimation of displacement even where the signal remains coherent. These track-specific expressions motivate our masking choices and should inform uncertainty interpretation on a per-track basis.

23335084, 2026, 8, Downloaded from https://agupubs.onlinelibrary.wiley.com/doi/10.1029/2026EA005214, Wiley Online Library on [29/09/2026]. See the Terms and Conditions (https://onlinelibrary.wiley.com/terms-and-conditions) on Wiley Online Library for rules of use; OA articles are governed by the applicable Creative Commons License

23335084, 2026, 8, Downloaded from https://agupubs.onlinelibrary.wiley.com/doi/10.1029/2026EA005214, Wiley Online Library on [29/09/2026]. See the Terms and Conditions (https://onlinelibrary.wiley.com/terms-and-conditions) on Wiley Online Library for rules of use; OA articles are governed by the applicable Creative Commons License

4.1.2. Residual Tropospheric Noise

Turbulent and stratified tropospheric delays add short- to long-wavelength phase perturbations that vary with acquisition time and boundary-layer state. Sentinel-1 ascending scenes over California are acquired in the early evening (∼18:05 PST), when surface heating and convective boundary-layer turbulence generally maximize small-scale water-vapor variability; descending scenes are acquired near dawn (∼06:15 PST), when the boundary layer is shallow and often more stratified (Stephens et al., 2020; Tomic, 2011). In our data, this diurnal sampling difference is evident: uncorrected ascending velocities exhibit larger long-wavelength structure and higher uncertainties than uncorrected descending results; applying weather-model tropospheric corrections reduces these discrepancies and flattens long-wavelength bias, bringing the two geometries to comparable uncertainty levels (Figures 1–3; see also Section 3.2). Li et al. (2005) and Murray et al. (2019) showed that statistical assessments and weather-model corrections reduce InSAR time-series bias and improve agreement with GNSS in continental settings; we observe the same qualitative behavior statewide (scatter reduction in Figure 6) and incorporate such corrections throughout our workflow.

Despite applying model-based corrections, we cannot fully reconcile residual, primarily turbulent, tropospheric noise—especially in evening (ascending) scenes where sub-10 km variability is largest. Our workflow treats a static acquisition-time correction per scene; it does not estimate intra-scene or pixel-dependent timing drifts, nor does it explicitly model day–night boundary-layer transitions. Consequently, short-wavelength residuals persist in some tracks (most notably in ascending over mountain fronts and coastal humidity gradients), and we caution that apparent long-wavelength signals at amplitudes $\leq$1 mm/yr may reflect imperfect removal of diurnally modulated tropospheric structure rather than geophysical deformation. Empirically, the evening–morning asymmetry in raw uncertainties largely collapses after tropospheric correction (Figure 2), but localized turbulent remnants remain and should be considered when interpreting broad, low-amplitude trends (Figure 6 and Section 3.2).

4.1.3. Reference Point Effects

For each InSAR track, we select reference points by inspecting GNSS time series in highly coherent (>0.75) areas to identify stable sites with minimal long-term deformation (e.g., velocity <1–2 mm/yr). This procedure is driven by manual inspection and assumes the site is effectively stable. In practice, however, even small residual motion at the reference location will be mapped onto the entire velocity field through the referencing step. As a result, any non-zero deformation at the reference point introduces a spatially uniform bias in the LOS velocity field. However, due to the side-looking geometry of radar satellites, the projection of three-dimensional ground motion into the LOS varies across the swath, with incidence angle increasing from near to far range (e.g., Figure 2). At smaller incidence angles (near range), LOS measurements are more sensitive to vertical motion, whereas at larger incidence angles (far range), sensitivity shifts toward horizontal (east–west) motion (Zebker et al., 1994). Consequently, while the reference-point bias is uniform in LOS, its impact may appear spatially variable when interpreted in the context of underlying deformation fields, particularly for large-scale horizontal motions that can produce ramp-like patterns in the velocity field. Because polar-orbiting satellites move nearly parallel to the Earth's meridians, LOS observations are insensitive to north-south displacements. Our vertical deformation interpretations across the Central Valley in particular assume minimal north-south motion, a simplification strongly validated by the close spatial agreement with localized ground positions. Deformation at the reference point and other locations may project differently into the observed displacement field depending on their range position. In addition, correlation and phase stability often degrade in the far range due to stronger geometric distortions, which can increase the risk of unwrapping errors if the reference point is poorly chosen (Hanssen, 2001). For these reasons, reference points are ideally selected in high-correlation areas, typically in near- to mid-range, where phase is stable and the incidence angle provides a balanced sensitivity to vertical and horizontal motion.

However, for our analysis we selected reference points from overlapping regions that fall in the near range of one track and the far range of another, which allowed us to directly link and "nest" adjacent interferometric tracks into a consistent regional framework. The key motivation for this approach is that overlapping zones provide common ground control, ensuring that relative phase offsets between tracks are removed. While incidence angle differences imply that each overlapping track has slightly different sensitivities to vertical versus horizontal motion, this primarily affects the decomposition of LOS displacement rather than the relative consistency of interferometric phase across the overlap (Zebker et al., 1994). To achieve seamless cross-track alignment, reference point

23335084, 2026, 8, Downloaded from https://agupubs.onlinelibrary.wiley.com/doi/10.1029/2026EA005214, Wiley Online Library on [29/09/2026]. See the Terms and Conditions (https://onlinelibrary.wiley.com/terms-and-conditions) on Wiley Online Library for rules of use; OA articles are governed by the applicable Creative Commons License

coordinates were optimized through iterative trial-and-error experimentation across the swath overlap boundaries. This empirical selection process balanced local lookup variations by testing reference sites against adjacent stable ground positions, preventing the propagation of uncorrected spatial ramps across the regional mosaic as illustrated in Figure S3 of Supporting Information S1. By manually shifting coordinates across shared, stable bedrock thresholds, step offsets are structurally minimized without warping the broader velocity field solutions.

4.2. Deviations From Linear, Secular Velocities

While long-term InSAR velocity observations provide valuable insights into secular deformation, they are complicated by deviations associated with earthquakes, hydrological variations, and other transient and non-linear processes. To account for such complexities, we fit for annual and semiannual seasonal parameters as well as Heaviside step parameters, the latter of which are commonly used to model coseismic offsets in time-series analyses (e.g., Yunjun et al., 2019). The 2019 Ridgecrest earthquake sequence provides a prime example: multiple Sentinel-1 tracks intersect the epicentral region, and abrupt displacements appear clearly in both ascending and descending LOS data. To extend velocity fields across this interval, coseismic steps were introduced into the time-series fits. Similar corrections were applied for the M6.5 Monte Cristo Range earthquake of 15 May 2020 and the M6.0 Antelope Valley earthquake of 8 July 2021 for all tracks which intersect with their respective epicentral regions. While these approaches stabilize the far-field secular trends, they cannot fully capture ongoing non-linear deformation in the near-field, where postseismic afterslip, viscoelastic relaxation, or poroelastic rebound may persist for years after large earthquakes (Fialko, 2004; Pollitz et al., 2001).

Comparisons of pre- and post-Ridgecrest velocity fields demonstrate this divergence clearly (Figure 7). Velocity differences are largest within the epicentral area, confirming that the main deviations are confined to regions proximal to the rupture (Xu et al., 2020). However, applying a uniform step function across entire tracks can create artifacts, as far-field areas remain stable and should not be forced into the same offset as the near-field. This mismatch underscores the need to test alternative modeling strategies that isolate earthquake-affected zones rather than imposing a single correction across broad swaths. At the same time, LOS differences highlight other non-seismic signals superimposed on long-term velocities. For example, drought-related subsidence in the Central Valley, transitioning to relative uplift during wetter periods, is consistent with independent hydrological studies (Carlson et al., 2020; Neely et al., 2021). Anomalous features near the Salton Trough, particularly in descending track geometries, remain less well understood; comparisons with vertical land motion estimates suggest the need for closer evaluation of uncertainties in that region (Govorcin et al., 2025).

These findings underscore that statewide velocity products, though robust at regional scales, require careful interpretation in zones of recent seismic activity. Hybrid modeling approaches that incorporate coseismic steps, hydrologically driven non-linear changes, and postseismic transients may provide more accurate representations of earthquake-cycle processes and other transient geophysical signals. Explicitly addressing the limitations of whole-track step fits, while leveraging regionally targeted models, will improve both the fidelity of transient signal characterization and the reliability of secular velocity fields for longer-term tectonic interpretations.

4.3. Best Practices for Producing Regional-Scale InSAR Velocity Maps and Future Efforts

Our California-wide InSAR velocity analysis has highlighted a number of best practices that should guide future efforts. Chief among these is the systematic incorporation of correction layers to mitigate atmospheric and geophysical noise sources. Previous studies have shown that ionospheric, tropospheric, and solid Earth tide corrections can significantly reduce long-wavelength biases that otherwise obscure tectonic signals (Fattahi et al., 2017; Hanssen, 2001; Yunjun et al., 2022). Such correction layers are included in the latest ARIA-S1-GUNW product processing campaigns in the region. While these layers are packaged in recent production campaigns, they were not leveraged in this study. Long wavelength phase variations were instead mitigated through external weather model tropospheric corrections, network baseline adjustments, and empirical reference frame nesting. Continued work leveraging ionospheric and solid Earth tide corrections was limited in this effort, subject to future funding and data access priorities. Because uncorrected ionospheric noise predominantly maps into broad, regional trends, its presence introduces minor spatial ramps across long distances without compromising the accuracy of short-to-intermediate wavelength signals, between 0.1 and 50 km (Figure S1 in Supporting Information S1), where our local deformation interpretations are focused. In parallel, the adoption of stitching workflows that emphasize consistency across overlapping scenes has proven critical, with qualitative rejection of

problematic interferograms, such as those dominated by decorrelation, unwrapping errors, or excessive atmospheric noise, emerging as an essential step to preserve product reliability (Yunjun et al., 2019; Zebker & Villasenor, 1992). Together, these practices help ensure that final velocity fields capture legitimate surface deformation signals rather than data artifacts.

The community, along with this data set, has also benefited from rigorous cross-validation strategies. Aligning InSAR-derived velocities with GNSS reference frames remains a best practice, allowing independent checks on both long-wavelength accuracy and temporal stability (Xu et al., 2021). Further, comparative analyses conducted within the SCEC Community Geodetic Model (CGM) InSAR working group—where multiple groups contribute independent solutions spanning the same region—have underscored the importance of methodological diversity. These inter-comparisons reveal the sensitivity of velocity fields to choices in time-series algorithms (e.g., SBAS vs. covariance-based methods) and highlight the value of a consensus framework (Berardino et al., 2002; Tymofyeyeva et al., 2023).

Building on these best practices, the OPERA DISP product suite represents a major step toward operational, continental-scale InSAR monitoring. Its hybrid Persistent Scatterer/Distributed Scatterer approach and inclusion of dedicated ionosphere and solid earth tide correction layers, along with the complementary OPERA TROPO product intended to correct for tropospheric noise, will standardize best practices at the product level, enabling more robust, reliable deformation analyses (Staniewicz et al., 2026). With low latency and open-access distribution, DISP will also facilitate rapid adoption into community workflows. Lessons from Ridgecrest also highlight the importance of these forthcoming standardized correction layers and covariance-based approaches within DISP products, which are expected to better manage such non-linearities and enhance future statewide velocity mapping. Future extensions, including vertical land motion products and incorporation of NISAR data, promise further advances by enabling pixel-level timing precision and decomposition of three-dimensional displacements (Govorcin et al., 2025).

Support for NISAR GUNW products has been implemented in the ARIA-tools software by the authors and collaborators, enabling downloading and preparation of NISAR data for time-series analysis. As with ARIA-S1-GUNWs, ARIA-tools provides command-line utilities to access NISAR interferograms, mosaic and crop scenes, extract auxiliary layers, and prepare the data for ingestion into community time-series processing workflows such as MintPy. Because the interface remains agnostic between Sentinel-1 and NISAR inputs, existing time-series processing pipelines and training materials translate directly to NISAR analysis efforts, enabling rapid community adoption and facilitating future statewide deformation analyses using the methods presented in this study.

Finally, the integration of these products into the CGM and related initiatives underscores the importance of sustained collaboration. Our contributions to both the ARIA and OPERA projects have directly supported consensus velocity models, fault creep surveys, and vertical land motion analyses (Floyd et al., 2023; Funning & Bürgmann, 2020; Govorcin et al., 2025). By continuing to align methodological refinements with community-wide standards, we help ensure that future InSAR velocity fields will not only be more accurate, but also more broadly usable across seismic hazard analyses and geophysical research. In this way, the lessons learned here extend beyond southern California, offering a template for regional-scale InSAR velocity mapping worldwide.

Conflict of Interest

The authors declare no conflicts of interest relevant to this study.

Availability Statement

The ARIA-tools (https://github.com/aria-tools/ARIA-tools) time-series preparation and MintPy (https://github.com/insarlab/MintPy.git) time-series analysis software package are both free and open-source. OPERA, managed by the Jet Propulsion Laboratory and funded by the Satellite Needs Working Group, is creating remote sensing products to address Earth observation needs across U.S. civilian federal agencies. To access the dataset, stable clones of the ARIA-tools and MintPy software, and associated user inputs needed to regenerate the dataset, refer to Sangha et al. (2026).

23335084, 2026, 8, Downloaded from https://agupubs.onlinelibrary.wiley.com/doi/10.1029/2026EA005214, Wiley Online Library on [29/09/2026]. See the Terms and Conditions (https://onlinelibrary.wiley.com/terms-and-conditions) on Wiley Online Library for rules of use; OA articles are governed by the applicable Creative Commons License

Acknowledgments
We thank M. Grace Bato and Jinwoo Kim for their developments which were leveraged in our validation workflow. We have also benefitted from numerous discussions on InSAR time series methodology and validation with Katia Tymofyeyeva, Mike Floyd, Xiaohua Xu, Kathryn Materna, Katherine Guns, Zhen Liu and Kang Wang. This research was supported by a Research Opportunities in Space and Earth Science (ROSES) Earth Surface and Interior (ESI) funded effort and the Statewide California Earthquake Center through awards 20177, 21035, 22049, 22059, 23109, 24081 and 25141. SCEC is funded by NSF Cooperative Agreement EAR-2225216 and USGS Cooperative Agreement G24AC00072. Additional support was provided by NASA Grant 80NSSC19K0739. This is SCEC Contribution 15010. We thank the Nevada Geodetic Laboratory for maintaining and providing free and open-access to their GNSS repository (Blewitt et al., 2018). The ARIA-S1-GUNW and OPERA DISP from Sentinel-1 (DISP-S1) products are free and openly available at the ASF DAAC. Users may request additional ARIA-S1-GUNW products beyond the current archive spatiotemporal coverage using ASF's free and open-source On-Demand service. The ARIA-S1-GUNW contains modified Copernicus Sentinel data. The DEM used during processing was modified to be a combination of the Copernicus DEM 30-m and Copernicus DEM 90-m models provided by the European Space Agency. The Copernicus DEM 30-m and Copernicus DEM 90-m were produced using Copernicus WorldDEM-30 © DLR e.V. 2010–2014 and © Airbus Defence and Space GmbH 2014–2018 provided under COPERNICUS by the European Union and ESA; all rights reserved. This study uses modified Copernicus Climate Change Service (C3S) ERA5 data provided by the European Centre for Medium-Range Weather Forecasts (ECMWF); neither the European Commission nor ECMWF is responsible for any use that may be made of the information. The research was carried out at the Jet Propulsion Laboratory, California Institute of Technology, under a contract with the National Aeronautics and Space Administration (80NM0018D0004).

References

Alaska Satellite Facility. (2026). ARIA Sentinel-1 GUNW product guide. Retrieved from https://hyp3-docs.asf.alaska.edu/guides/gunw_product_guide/

Argus, D. F., Heflin, M. B., Peltzer, G., Crampé, F., & Webb, F. H. (2005). Interseismic strain accumulation and anthropogenic motion in metropolitan Los Angeles. *Journal of Geophysical Research*, *110*(B4), B04401. https://doi.org/10.1029/2003jb002934

ARIA Project. (2026). Advanced rapid imaging and analysis (ARIA) [Dataset]. *NASA Earthdata*. Retrieved from https://www.earthdata.nasa.gov/data/projects/aria

Bawden, G. W., Thatcher, W., Stein, R. S., Hudnut, K. W., & Peltzer, G. (2001). Tectonic contraction across Los Angeles after removal of groundwater pumping effects. *Nature*, *412*(6849), 812–815. https://doi.org/10.1038/35090558

Bekaert, D. P., Jones, C. E., An, K., & Huang, M. H. (2019). Exploiting UAVSAR for a comprehensive analysis of subsidence in the Sacramento Delta. *Remote Sensing of Environment*, *220*, 124–134. https://doi.org/10.1016/j.rse.2018.10.023

Bekaert, D. P. S., Hooper, A., & Wright, T. J. (2015). Reassessing the 2006 Guerrero slow-slip event, Mexico: Implications for large earthquakes in the Guerrero gap. *Journal of Geophysical Research: Solid Earth*, *120*(2), 1357–1375. https://doi.org/10.1002/2014jb011557

Bekaert, D. P. S., Walters, R. J., Wright, T. J., Hooper, A. J., & Parker, D. J. (2015). Statistical comparison of InSAR tropospheric correction techniques. *Remote Sensing of Environment*, *170*, 40–47. https://doi.org/10.1016/j.rse.2015.08.035

Berardino, P., Fornaro, G., Lanari, R., & Sansosti, E. (2002). A new algorithm for surface deformation monitoring based on small baseline differential SAR interferograms. *IEEE Transactions on Geoscience and Remote Sensing*, *40*(11), 2375–2383. https://doi.org/10.1109/tgrs.2002.803792

Biggs, J., Wright, T., Lu, Z., & Parsons, B. (2007). Multi-interferogram method for measuring interseismic deformation: Denali Fault, Alaska. *Geophysical Journal International*, *170*(3), 1165–1179. https://doi.org/10.1111/j.1365-246x.2007.03415.x

Blewitt, G., Hammond, W. C., & Kreemer, C. (2018). Harnessing the GPS data explosion for interdisciplinary science. *Eos*, *99*. https://doi.org/10.1029/2018eo104623

Bock, Y., & Melgar, D. (2016). Physical applications of GPS geodesy: A review. *Reports on Progress in Physics*, *79*(10), 106801. https://doi.org/10.1088/0034-4885/79/10/106801

Bürgmann, R., Hilley, G., Ferretti, A., & Novali, F. (2006). Resolving vertical tectonics in the San Francisco Bay Area from permanent scatterer InSAR and GPS analysis. *Geology*, *34*(3), 221–224. https://doi.org/10.1130/g22064.1

Bürgmann, R., Rosen, P. A., & Fielding, E. J. (2000). Synthetic aperture radar interferometry to measure Earth's surface topography and its deformation. *Annual Review of Earth and Planetary Sciences*, *28*(1), 169–209. https://doi.org/10.1146/annurev.earth.28.1.169

Bürgmann, R., Schmidt, D., Nadeau, R. M., d'Alessio, M., Fielding, E. J., Manaker, D., et al. (2000). Earthquake potential along the Northern Hayward fault, California. *Science*, *289*(5482), 1178–1182. https://doi.org/10.1126/science.289.5482.1178

Buzzanga, B., Bekaert, D. P., Hamlington, B. D., & Sangha, S. S. (2020). Towards sustained monitoring of subsidence at the coast using InSAR and GPS: An application in Hampton Roads, Virginia. *Geophysical Research Letters*, *47*(18), e2020GL090013. https://doi.org/10.1029/2020gl090013

Carlson, G., Shirzaei, M., Ojha, C., & Werth, S. (2020). Subsidence-derived volumetric strain models for mapping extensional fissures and constraining rock mechanical properties in the San Joaquin Valley, California. *Journal of Geophysical Research: Solid Earth*, *125*(9), e2020JB019980. https://doi.org/10.1029/2020jb019980

Chen, C. W., & Zebker, H. A. (2002). Phase unwrapping for large SAR interferograms: Statistical segmentation and generalized network models. *IEEE Transactions on Geoscience and Remote Sensing*, *40*(8), 1709–1719. https://doi.org/10.1109/tgrs.2002.802453

Dong, D., Fang, P., Bock, Y., Cheng, M. K., & Miyazaki, S. I. (2002). Anatomy of apparent seasonal variations from GPS-derived site position time series. *Journal of Geophysical Research*, *107*(B4), 2075. https://doi.org/10.1029/2001JB000573

Efron, B., & Tibshirani, R. (1986). Bootstrap methods for standard errors, confidence intervals, and other measures of statistical accuracy. *Statistical Science*, *1*(1), 54–75. https://doi.org/10.1214/ss/1177013815

Fattahi, H., & Amelung, F. (2015). InSAR bias and uncertainty due to the systematic and stochastic tropospheric delay. *Journal of Geophysical Research: Solid Earth*, *120*(12), 8758–8773. https://doi.org/10.1002/2015JB012419

Fattahi, H., Simons, M., & Agram, P. (2017). InSAR time-series estimation of the ionospheric phase delay: An extension of the split range-spectrum technique. *IEEE Transactions on Geoscience and Remote Sensing*, *55*(10), 5984–5996. https://doi.org/10.1109/TGRS.2017.2718566

Ferretti, A., Prati, C., & Rocca, F. (2001). Permanent scatterers in SAR interferometry. *IEEE Transactions on Geoscience and Remote Sensing*, *39*(1), 8–20. https://doi.org/10.1109/36.898661

Fialko, Y. (2004). Evidence of fluid-filled upper crust from observations of postseismic deformation due to the 1992 M7.3 Landers earthquake. *Journal of Geophysical Research*, *109*, B08401.

Fialko, Y. (2006). Interseismic strain accumulation and the earthquake potential on the southern San Andreas fault system. *Nature*, *441*(7096), 968–971. https://doi.org/10.1038/nature04797

Fielding, E. J., Blom, R. G., & Goldstein, R. M. (1998). Rapid subsidence over oil fields measured by SAR interferometry. *Geophysical Research Letters*, *25*(17), 3215–3218. https://doi.org/10.1029/98gl52260

Fielding, E. J., Talebian, M., Rosen, P. A., Nazari, H., Jackson, J. A., Ghorashi, M., & Walker, R. (2005). Surface ruptures and building damage of the 2003 Bam, Iran, earthquake mapped by satellite synthetic aperture radar interferometric correlation. *Journal of Geophysical Research*, *110*(B3), B03302. https://doi.org/10.1029/2004jb003299

Floyd, M. A., Tymofyeyeva, E., Materna, K., Bekaert, D. P., Fielding, E. J., Funning, G. J., et al. (2023). Southern California Earthquake Center (SCEC) Community Geodetic Model (CGM) (Version 2.0.0) [Dataset]. *Zenodo*. https://doi.org/10.5281/zenodo.10076838

Floyd, M. A., Walters, R. J., Elliott, J. R., Funning, G. J., Svarc, J. L., Murray, J. R., et al. (2016). Spatial variations in fault friction related to lithology from rupture and afterslip of the 2014 South Napa, California, earthquake. *Geophysical Research Letters*, *43*(13), 6808–6816. https://doi.org/10.1002/2016gl069428

Funning, G., & Bürgmann, R. (2020). *The importance of expanding the Earthquake Center region to include the northern San Andreas fault system*. SCEC White Paper. Retrieved from https://scholar.google.com/citations?view_op=view_citation&hl=en&user=vraY0G0AAAAJ&cstart=20&pagesize=80&sortby=pubdate&citation_for_view=vraY0G0AAAAJ:ZfRJV9d4-WMC

Funning, G. J., Bürgmann, R., Ferretti, A., Novali, F., & Fumagalli, A. (2007). Creep on the Rodgers Creek fault, northern San Francisco Bay area from a 10 year PS-InSAR dataset. *Geophysical Research Letters*, *34*(19), L19306. https://doi.org/10.1029/2007gl030836

Funning, G. J., & Garcia, A. (2019). A systematic study of earthquake detectability using Sentinel-1 Interferometric Wide-Swath data. *Geophysical Journal International*, *216*(1), 332–349. https://doi.org/10.1093/gji/ggy426

Gabriel, A. K., Goldstein, R. M., & Zebker, H. A. (1989). Mapping small elevation changes over large areas: Differential radar interferometry. *Journal of Geophysical Research*, *94*(B7), 9183–9191. https://doi.org/10.1029/jb094ib07p09183

23335084, 2026, 8, Downloaded from https://agupubs.onlinelibrary.wiley.com/doi/10.1029/2026EA005214, Wiley Online Library on [29/09/2026]. See the Terms and Conditions (https://onlinelibrary.wiley.com/terms-and-conditions) on Wiley Online Library for rules of use; OA articles are governed by the applicable Creative Commons License

Govorcin, M., Bekaert, D. P. S., Hamlington, B. D., Sangha, S. S., & Sweet, W. (2025). Variable vertical land motion and its impacts on sea level rise projections. *Science Advances*, *11*(5), eads8163. https://doi.org/10.1126/sciadv.ads8163

Handwerger, A. L., Fielding, E. J., Sangha, S. S., & Bekaert, D. P. (2022). Landslide sensitivity and response to precipitation changes in wet and dry climates. *Geophysical Research Letters*, *49*(13), e2022GL099499. https://doi.org/10.1029/2022gl099499

Handwerger, A. L., Roering, J. J., & Schmidt, D. A. (2013). Controls on the seasonal deformation of slow-moving landslides. *Earth and Planetary Science Letters*, *377–378*, 239–247. https://doi.org/10.1016/j.epsl.2013.06.047

Hanssen, R. F. (2001). *Radar interferometry: Data interpretation and error analysis*. Springer.

Hilley, G. E., Bürgmann, R., Ferretti, A., Novali, F., & Rocca, F. (2004). Dynamics of slow-moving landslides from permanent Scatterer analysis. *Science*, *304*(5679), 1952–1955. https://doi.org/10.1126/science.1098821

Hogenson, K., Kristenson, H., Kennedy, J., Johnston, A., Rine, J., Logan, T., et al. (2020). Hybrid Pluggable Processing Pipeline (HyP3): A cloud-native infrastructure for generic processing of SAR data [Software]. *Zenodo*. https://doi.org/10.5281/zenodo.4646138

Hooper, A., Bekaert, D., Spaans, K., & Arıkan, M. (2012). Recent advances in SAR interferometry time series analysis for measuring crustal deformation. *Tectonophysics*, *514*, 1–13. https://doi.org/10.1016/j.tecto.2011.10.013

Johanson, I. A., Fielding, E. J., Rolandone, F., & Bürgmann, R. (2006). Coseismic and postseismic slip of the 2004 Parkfield earthquake from space-geodetic data. *Bulletin of the Seismological Society of America*, *96*, S269–S282.

Jolivet, R., Grandin, R., Lasserre, C., Doin, M.-P., & Peltzer, G. (2011). Systematic InSAR tropospheric phase delay corrections from global meteorological reanalysis data. *Geophysical Research Letters*, *38*(17), L17311. https://doi.org/10.1029/2011gl048757

Jolivet, R., Simons, M., Agram, P. S., Duputel, Z., & Shen, Z.-K. (2015). Aseismic slip and seismogenic coupling along the central San Andreas Fault. *Geophysical Research Letters*, *42*(2), 297–306. https://doi.org/10.1002/2014gl062222

Jones, J., Jones, C. E., & Bekaert, D. P. (2022). Value of InSAR for monitoring land subsidence to support water management in the San Joaquin Valley, California. *Journal of the American Water Resources Association*, *58*(6), 995–1001. https://doi.org/10.1111/1752-1688.12942

Lanari, R., Lundgren, P., Manzo, M., & Casu, F. (2004). Satellite radar interferometry time series analysis of surface deformation for Los Angeles, California. *Geophysical Research Letters*, *31*(23). https://doi.org/10.1029/2004gl021294

Langbein, J., & Johnson, H. (1997). Correlated errors in geodetic time series: Implications for time-dependent deformation. *Journal of Geophysical Research*, *102*(B1), 591–603. https://doi.org/10.1029/96jb02945

Li, X., Handwerger, A. L., Peltzer, G., & Fielding, E. (2024). Exploring the behaviors of initiated progressive failure and slow-moving landslides in Los Angeles using satellite InSAR and pixel offset tracking. *Geophysical Research Letters*, *51*(13), e2024GL108267. https://doi.org/10.1029/2024gl108267

Li, Z., Muller, J.-P., Cross, P., & Fielding, E. J. (2005). Interferometric synthetic aperture radar (InSAR) atmospheric correction: GPS, MODIS, and InSAR integration. *Journal of Geophysical Research*, *110*, B03410.

Lohman, R. B., & McGuire, J. J. (2007). Earthquake swarms driven by aseismic creep in the Salton Trough, California. *Journal of Geophysical Research*, *112*(B4), B04405. https://doi.org/10.1029/2006jb004596

Mao, A., Harrison, C. G. A., & Dixon, T. H. (1999). Noise in GPS coordinate time series. *Journal of Geophysical Research*, *104*(B2), 2797–2816. https://doi.org/10.1029/1998jb900033

Massonnet, D., Rossi, M., Carmona, C., Adragna, F., Peltzer, G., Feigl, K. L., & Rabaute, T. (1993). The displacement field of the Landers earthquake mapped by radar interferometry. *Nature*, *364*(6433), 138–142. https://doi.org/10.1038/364138a0

Miller, M. M., Jones, C. E., Sangha, S. S., & Bekaert, D. P. (2020). Rapid drought-induced land subsidence and its impact on the California aqueduct. *Remote Sensing of Environment*, *251*, 112063. https://doi.org/10.1016/j.rse.2020.112063

Murray, K. D., Bekaert, D. P., & Lohman, R. B. (2019). Tropospheric corrections for InSAR: Statistical assessments and applications to the Central United States and Mexico. *Remote Sensing of Environment*, *232*, 111326. https://doi.org/10.1016/j.rse.2019.111326

NASA/JPL/OPERA. (2025). OPERA Surface Displacement from Sentinel-1 validated product (Version 1) [Dataset]. *NASA Alaska Satellite Facility*. https://doi.org/10.5067/SNWG/OPL3DISPS1-V1

Neely, W. R., Borsa, A. A., Burney, J. A., Levy, M. C., Silverii, F., & Sneed, M. (2021). Characterization of groundwater recharge and flow in California's San Joaquin Valley from InSAR-observed surface deformation. *Water Resources Research*, *57*(4), e2020WR028451. https://doi.org/10.1029/2020wr028451

NISAR, ATBD Notebooks. (2024). Notebooks for NISAR solid Earth Algorithm theoretical basis document [Software]. *GitHub*. https://github.com/nisar-solid/ATBD

NISAR ATBD Review. (2024). The NISAR Algorithm theoretical basis document review [Dataset]. *GitLab*. Retrieved from https://gitlab.com/nisar-science-algorithms/atbd-review-overview

Peltzer, G., Crampé, F., Hensley, S., & Rosen, P. (2001). Transient strain accumulation and fault interaction in the Eastern California shear zone. *Geology*, *29*(11), 975–978. https://doi.org/10.1130/0091-7613(2001)029<0975:tsaafi>2.0.co;2

Poland, J. F., Lofgren, B. E., Ireland, R. L., & Pugh, R. G. (1975). *Land subsidence in the San Joaquin Valley, California, as of 1972* (pp. 437–H). USGS Professional Paper.

Pollitz, F. F., Wicks, C., & Thatcher, W. (2001). Mantle flow beneath a Continental strike-slip fault: Postseismic deformation after the 1999 hector mine earthquake. *Science*, *293*(5536), 1814–1818. https://doi.org/10.1126/science.1061361

Riel, B., Simons, M., Ponti, D., Agram, P., & Jolivet, R. (2018). Quantifying ground deformation in the Los Angeles and Santa Ana Coastal Basins due to groundwater withdrawal. *Water Resources Research*, *54*(5), 3557–3582. https://doi.org/10.1029/2017wr021978

Rodriguez, E., & Martin, J. M. (1992). Theory and design of interferometric synthetic aperture radars. *IEEE Proceedings F—Radar and Signal Processing*, *139*(2), 147–159. https://doi.org/10.1049/ip-f-2.1992.0018

Rosen, P. A., Hensley, S., Joughin, I. R., Li, F. K., Madsen, S. N., Rodríguez, E., & Goldstein, R. M. (2000). Synthetic aperture radar interferometry. *Proceedings of the IEEE*, *88*(3), 333–382. https://doi.org/10.1109/5.838084

Ryder, I., & Bürgmann, R. (2008). Spatial variations in slip deficit on the central San Andreas Fault from InSAR. *Geophysical Journal International*, *175*(3), 837–852. https://doi.org/10.1111/j.1365-246x.2008.03938.x

Salvi, S., Stramondo, S., Funning, G. J., Ferretti, A., Sarti, F., & Mouratidis, A. (2012). The Sentinel-1 mission for the improvement of the scientific understanding and the operational monitoring of the seismic cycle. *Remote Sensing of Environment*, *120*, 164–174. https://doi.org/10.1016/j.rse.2011.09.029

Sangha, S. S., Funning, G., Govorcin, M., & Bekaert, D. (2026). Data and software for Sangha et al., 2026: A statewide InSAR velocity map for California produced by a comprehensive large scale analysis of ARIA standard products [submitted for publication] [Dataset]. *Zenodo*. https://doi.org/10.5281/zenodo.19493073

Schmidt, D. A., & Bürgmann, R. (2003). Time-dependent land uplift and subsidence in the Santa Clara valley, California, from a large interferometric synthetic aperture radar data set. *Journal of Geophysical Research*, *108*(B9), 2416. https://doi.org/10.1029/2002jb002267

23335084, 2026, 8, Downloaded from https://agupubs.onlinelibrary.wiley.com/doi/10.1029/2026EA005214, Wiley Online Library on [29/09/2026]. See the Terms and Conditions (https://onlinelibrary.wiley.com/terms-and-conditions) on Wiley Online Library for rules of use; OA articles are governed by the applicable Creative Commons License

Schmidt, D. A., Bürgmann, R., Nadeau, R. M., & d'Alessio, M. (2005). Distribution of aseismic slip rate on the Hayward fault inferred from seismic and geodetic data. *Journal of Geophysical Research*, *110*(B8), B08406. https://doi.org/10.1029/2004jb003397

Shirzaei, M., & Bürgmann, R. (2018). Global climate change and local land subsidence exacerbate inundation risk to the San Francisco Bay Area. *Science Advances*, *4*(3), eaap9234. https://doi.org/10.1126/sciadv.aap9234

Simons, M., Bekaert, D. P., Hensley, S., Lavalle, M., Lundgren, P. R., Milillo, P., et al. (2021). Nisar requirements and validation approach for solid earth science. In *2021 IEEE International Geoscience and Remote Sensing Symposium IGARSS* (pp. 543–546).

Smith, R. G., Knight, R., Chen, J., Reeves, J. A., Zebker, H. A., Farr, T., & Liu, Z. (2017). Estimating the permanent loss of groundwater storage in the southern San Joaquin Valley, California. *Water Resources Research*, *53*, 2133–2148. https://doi.org/10.1002/2016WR019861

Staniewicz, S., Mirzaee, S., Fattahi, H., Oliver-Cabrera, T., Havazli, E., Gunter, G., et al. (2026). Near-Real-Time InSAR phase estimation for large-scale surface displacement monitoring. *IEEE Transactions on Geoscience and Remote Sensing*.

Stephens, K. J., Wauthier, C., Bussard, R. C., Higgins, M., & LaFemina, P. C. (2020). Assessment of mitigation strategies for tropospheric phase contributions to InSAR time-series datasets over two Nicaraguan volcanoes. *Remote Sensing*, *12*(5), 782. https://doi.org/10.3390/rs12050782

Tomic, J. (2011). *Observations and modeling of the current deformation in afar using synthetic aperture radar interferometry*. [Thesis]. University of California.

Tong, X., Sandwell, D. T., & Smith-Konter, B. (2013). High-resolution interseismic velocity data along the San Andreas Fault from GPS and InSAR. *Journal of Geophysical Research: Solid Earth*, *118*(1), 369–389. https://doi.org/10.1029/2012jb009442

Torres, R., Snoeij, P., Geudtner, D., Bibby, D., Davidson, M., Attema, E., et al. (2012). GMES Sentinel-1 mission. *Remote Sensing of Environment*, *120*, 9–24. https://doi.org/10.1016/j.rse.2011.05.028

Tymofyeyeva, E., & Fialko, Y. (2015). Mitigation of atmospheric phase delays in InSAR data, with application to the eastern California shear zone. *Journal of Geophysical Research: Solid Earth*, *120*(8), 5952–5963. https://doi.org/10.1002/2015jb011886

Tymofyeyeva, E., Floyd, M. A., Wang, K., Guns, K. A., Materna, K., Liu, Z., et al. (2023). InSAR community geodetic model version 2: Moving beyond Ridgecrest. In *Poster Presentation at 2023 SCEC Annual Meeting*.

U. S. Geological Survey. (2025a). San Andreas Bay Area faults [Dataset]. *Earthquake Hazards Program*. https://earthquake.usgs.gov/earthquakes/events/1906calif/virtualtour/kml/SanAndreas_BayAreaFaults.kmz

U. S. Geological Survey. (2025b). USGS shaded relief only [Dataset]. *The National Map*. https://basemap.nationalmap.gov/arcgis/rest/services/USGSShaded_Relief_Only/MapServer

Ulloa, N. I., Chiang, S.-H., & Yun, S.-H. (2020). Flood proxy mapping with normalized difference sigma-naught index and Shannon's entropy. *Remote Sensing*, *12*(9), 1384. https://doi.org/10.3390/rs12091384

Vasco, D. W., Rutqvist, J., Ferretti, A., Rucci, A., Bellacicco, F., Dobson, P. F., et al. (2013). Monitoring deformation at the Geysers Geothermal Field, California using C-band and X-band interferometric synthetic aperture radar. *Geophysical Research Letters*, *40*(11), 2567–2572. https://doi.org/10.1002/grl.50314

Wei, M., Sandwell, D., & Fialko, Y. (2009). A silent Mw 4.7 slip event of October 2006 on the Superstition Hills fault, southern California. *Journal of Geophysical Research*, *114*, B07402.

Wei, M., & Sandwell, D. T. (2010). Decorrelation of L-band and C-band interferometry over vegetated areas in California. *IEEE Transactions on Geoscience and Remote Sensing*, *48*(7), 2942–2952. https://doi.org/10.1109/tgrs.2010.2043442

Weiss, J. R., Walters, R. J., Morishita, Y., Wright, T. J., Lazecky, M., Wang, H., et al. (2020). High-resolution surface velocities and strain for Anatolia from Sentinel-1 InSAR and GNSS data. *Geophysical Research Letters*, *47*(17), e2020GL087376. https://doi.org/10.1029/2020gl087376

Wright, T. J., Parsons, B., & Fielding, E. J. (2001). Measurement of interseismic strain accumulation across the North Anatolian Fault by satellite radar interferometry. *Geophysical Research Letters*, *28*(10), 2117–2120. https://doi.org/10.1029/2000gl012850

Xu, X., Sandwell, D. T., Klein, E., & Bock, Y. (2021). Integrated Sentinel-1 InSAR and GNSS time-series along the San Andreas fault system. *Journal of Geophysical Research: Solid Earth*, *126*(11), e2021JB022579. https://doi.org/10.1029/2021JB022579

Xu, X., Sandwell, D. T., Ward, L. A., Milliner, C. W., Smith-Konter, B. R., Fang, P., & Bock, Y. (2020). Surface deformation associated with fractures near the 2019 Ridgecrest earthquake sequence. *Science*, *370*(6516), 605–608. https://doi.org/10.1126/science.abd1690

Yun, S.-H., Hudnut, K. W., Owen, S., Webb, F., Simons, M., Sacco, P., et al. (2015). Rapid damage mapping for the 2015 Mw 7.8 gorkha earthquake using synthetic aperture radar data from COSMO-SkyMed and ALOS-2 satellites. *Seismological Research Letters*, *86*(6), 1549–1556. https://doi.org/10.1785/0220150152

Yunjun, Z., Fattahi, H., & Amelung, F. (2019). Small baseline InSAR time series analysis: Unwrapping error correction and noise reduction. *Computers and Geosciences*, *133*, 104331. https://doi.org/10.1016/j.cageo.2019.104331

Yunjun, Z., Fattahi, H., Pi, X., Rosen, P., Simons, M., Agram, P., & Aoki, Y. (2022). Range geolocation accuracy of C-/L-band SAR and its implications for operational stack coregistration. *IEEE Transactions on Geoscience and Remote Sensing*, *60*, 1–19. https://doi.org/10.1109/tgrs.2022.3168509

Zanaga, D., Van De Kerchove, R., Daems, D., De Keersmaecker, W., Brockmann, C., Kirches, G., et al. (2022). ESA WorldCover 10 m 2021 v200 [Dataset]. *Zenodo*. https://doi.org/10.5281/zenodo.7254221

Zebker, H., & Villasenor, J. (1992). Decorrelation in interferometric radar echoes. *IEEE Transactions on Geoscience and Remote Sensing*, *30*(5), 950–959. https://doi.org/10.1109/36.175330

Zebker, H. A., Rosen, P. A., Goldstein, R. M., Gabriel, A., & Werner, C. L. (1994). On the derivation of coseismic displacement fields using differential radar interferometry: The landers earthquake. *Journal of Geophysical Research*, *99*(B10), 19617–19634. https://doi.org/10.1029/94jb01179

Zhang, J., Bock, Y., Johnson, H., Fang, P., Williams, S., Genrich, J., et al. (1997). Southern California permanent GPS geodetic array: Error analysis of daily position estimates and site velocities. *Journal of Geophysical Research*, *102*(B8), 18035–18055. https://doi.org/10.1029/97jb01380

23335084, 2026, 8, Downloaded from https://agupubs.onlinelibrary.wiley.com/doi/10.1029/2026EA005214, Wiley Online Library on [29/09/2026]. See the Terms and Conditions (https://onlinelibrary.wiley.com/terms-and-conditions) on Wiley Online Library for rules of use; OA articles are governed by the applicable Creative Commons License